

Embracing Imperfect Datasets: A Review of Deep Learning Solutions for Medical Image Segmentation

Nima Tajbakhsh, Laura Jeyaseelan, Qian Li, Jeffrey N. Chiang, Zhihao Wu, and Xiaowei Ding^a

^a*VoxelCloud, Inc.*

Abstract

The medical imaging literature has witnessed remarkable progress in high-performing segmentation models based on convolutional neural networks. Despite the new performance highs, the recent advanced segmentation models still require large, representative, and high quality annotated datasets. However, rarely do we have a perfect training dataset, particularly in the field of medical imaging, where data and annotations are both expensive to acquire. Recently, a large body of research has studied the problem of medical image segmentation with imperfect datasets, tackling two major dataset limitations: scarce annotations where only limited annotated data is available for training, and weak annotations where the training data has only sparse annotations, noisy annotations, or image-level annotations. In this article, we provide a detailed review of the solutions above, summarizing both the technical novelties and empirical results. We further compare the benefits and requirements of the surveyed methodologies and provide our recommended solutions. We hope this survey article increases the community awareness of the techniques that are available to handle imperfect medical image segmentation datasets.

Keywords: medical image segmentation, imperfect dataset, scarce annotations, noisy annotations, unreliable annotations, sparse annotations, and weak annotations

1. Introduction

Medical imaging literature has witnessed great progress in the designs and performance of deep convolutional models for medical image segmentation. Since the introduction of UNet [Ronneberger et al. \(2015\)](#), neural architectures for medical image segmentation have transformed markedly. State-of-the-art architectures now benefit from re-designed skip connections [Zhou et al. \(2018b\)](#), residual convolution blocks [Alom et al. \(2018\)](#), dense convolution blocks [Li et al. \(2018\)](#), attention mechanisms [Oktay et al. \(2018\)](#), hybrid squeeze-excitation modules [Roy et al. \(2018\)](#), to name a few. Although the architectural advancements have enabled new performance highs, they still require large, high-quality annotated datasets—more so than before.

However, rarely do we have a perfectly-sized and carefully-labeled dataset to train an image segmentation model, particularly for medical imaging applications, where both data and annotations are expensive to acquire. The common limitations of medical image segmentation datasets include scarce annotations where only limited annotated data is available for training, and weak annotations where the training data has only sparse annotations, noisy annotations, or image-level annotations. In the presence of these dataset shortcomings, even the most advanced segmentation models may fail to generalize to datasets from real-world clinical settings. In response to this challenge, researchers from the medical imaging community have actively sought solutions, resulting in a diverse and effective set of techniques with demonstrated capabilities in handling scarce and weak annotations for the

task of medical image segmentation. In this article, we have reviewed these solutions in depth, summarizing both the technical novelties and empirical results. We hope this review increases the community awareness of the existing solutions for the common limitations of medical image segmentation datasets, and further inspires the research community to explore solutions for the less explored dataset problems.

2. Related works

[Litjens et al. \(2017\)](#) surveyed the early deep learning solutions for various medical imaging applications including image classification, object detection, and object segmentation. Following this seminal survey, [Yi et al. \(2018\)](#) broadly investigated the use of generative adversarial networks (GANs) in medical imaging. [Cheplygina et al. \(2019\)](#) reviewed semi-supervised, multi-instance learning, and transfer learning in medical image analysis, covering both deep learning and traditional segmentation methods. The surveys by [Hesamian et al. \(2019\)](#); [Taghanaki et al. \(2019\)](#) reviewed deep learning techniques suggested for medical image segmentation but with a particular focus on architectural advancements and training schemes. The most relevant surveys to our work are [Zhang et al. \(2019b\)](#), which reviewed the solutions that tackle the small sample size problem for the broad medical image analysis, and [Karimi et al. \(2019\)](#) where the authors surveyed the methods suggested for handling label noise in both natural and medical image datasets.

In contrast, the current survey has focused on problems of scarce and weak annotations with respect to medical image

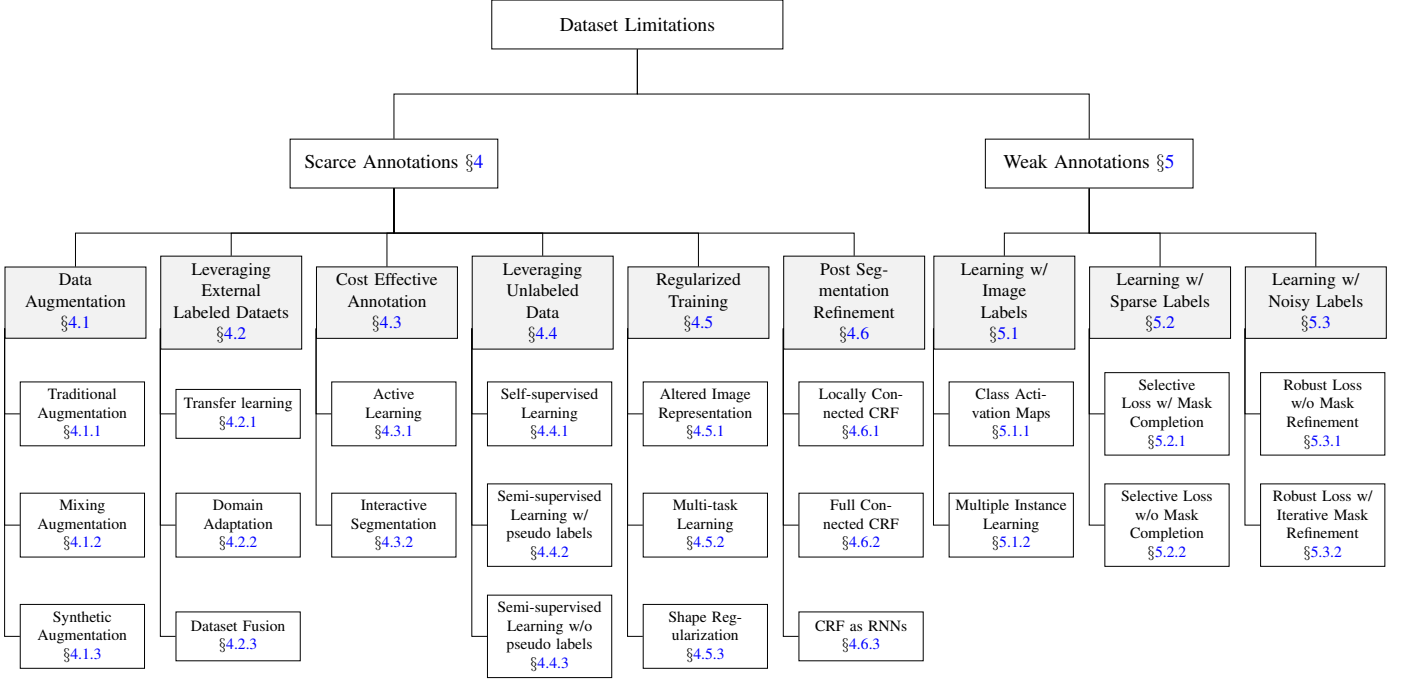


Figure 1: Organization of this review paper. We broadly categorize the limitations of medical image segmentation datasets into scarce annotations and weak annotations. For each problem, we then present the strategies (highlighted in grey) followed by the suggested solutions.

segmentation. Our focus is motivated by the fact that image segmentation requires the strongest supervision among other vision tasks such as classification and detection; and thus, most vulnerable to the quality and quantity of annotations. The specific scope and deep review of this survey distinguish it from [Yi et al. \(2018\)](#); [Cheplygina et al. \(2019\)](#) that broadly cover deep learning for general medical image analysis, from [Hesamian et al. \(2019\)](#) that focuses on architectural advancements for medical image segmentation, and from [Zhang et al. \(2019b\)](#) that investigates only the small sample size problem in medical image segmentation, and from the work of [Karimi et al. \(2019\)](#) that primarily considers label noise in the medical image datasets.

3. Organization of survey

Figure 1 shows the organization of this survey. We have broadly grouped limitations associated with medical image segmentation datasets into two sections: 1) scarce annotations (Section 4), which covers methodologies that can handle datasets where only a small fraction of images are densely annotated; and 2) weak annotations (Section 5), which covers methodologies that leverage datasets with sparse, noisy, or only image-level annotations.

The methodologies presented for scarce annotations in Section 4 are further grouped into three categories according to their methodology principles. The first category consists of the methods that aim to enlarge the training set (sections 4.1–4.4) through data augmentation, leveraging external but related labeled datasets, cost effective annotation, and leveraging unlabeled data. Although these methods share the same philos-

ophy, they differ in the required data resources and whether or not they require the expert in the loop. The second category (section 4.5) consists of methods that strengthen regularization during model training, where the regularization can be applied to the input space by changing the image representation, to the output space by constraining the segmentation results with shape priors, or directly to the gradients by leveraging additional supervision signals through multi-task learning. Except for multi-task learning, regularization-based methods do not require any further data or annotations. The third category consists of methods that aim to refine the segmentation mask (section 4.6) using different variants of conditional random fields (CRFs) either as a post-processing or during model training. These methods require no further data other than the currently available segmentation dataset.

The methodologies presented in Section 5 for the problem of weak annotations are further grouped by the type of annotation weakness into 3 sections: 1) methods that tackle image-level annotations (section 5.1), which use different variants of class activation maps to leverage weak image-level labels for medical image segmentation; 2) methods that leverage sparse annotations (section 5.2), which are typically based on some variants of selective loss where only sparsely labeled pixels contribute to the segmentation loss; 3) methods that handle noisy annotations (section 5.3), which typically use noise-resilient loss functions to learn from noisy annotations.

In section 6, we summarize this survey by comparing the methodologies under review from the perspectives of performance gain, implementation difficulty, and required data resources. We further provide our recommended solutions based on a cost-gain trade-off.

4. Problem I: Scarce annotation

Scarce annotation is a common problem when using supervised deep learning methods for medical image segmentation. Traditional solutions to this problem are data augmentation, transfer learning from natural images, and weight regularization. However, these techniques can only partially address the problem of limited annotation. For example, traditional data augmentation is handicapped by the large correlation between the original training set and the augmented examples. Transfer learning from natural images only benefits 2D medical image segmentation models, with no benefits to the common 3D medical image segmentation models.

The limited capability of the traditional methods in handling the problem of scarce annotations has led to the development of modern reactive and proactive approaches. The reactive methods tackle the problem of scarce annotation through a post segmentation refinement using variants of conditional random fields. The proactive approaches, on the other hand, actively enlarge the training set through cost-effective annotation and synthetic data generation or change the training paradigm by leveraging unlabeled data and using additional model regularization during training. In the following, we provide a comprehensive summary of such modern solutions to the ubiquitous problem of scarce annotations in medical image segmentation.

4.1. Data augmentation

Data augmentation has served as an effective solution to the problem of over-fitting, particularly in the absence of large labeled training sets. In this section, we cover the data augmentation methods based on traditional spatial and intensity transforms, data augmentation by mixing images, and modern image synthesis methods based on adversarial networks. While the scope of this section is limited to medical images, the readers can refer to the survey by [Shorten and Khoshgof-taar \(2019\)](#) for a comprehensive review of data augmentation methods for both natural and medical image domains.

4.1.1. Traditional Augmentation

Traditional data augmentation has proved effective in reducing over-fitting and improving test performance for both natural and medical images [Zhang et al. \(2016\)](#). The data augmentation methods used in medical imaging can be grouped by the image property they intend to manipulate [Zhang et al. \(2019a\)](#). These common image properties consists of image quality, image appearance, and image layout.

By image quality: Similar to the data augmentation for 2D natural images, image quality can be affected by sharpness, blurriness and noise. [Christ et al. \(2016\)](#) apply Gaussian noise to CT scans as part of data augmentation. [Sirinukunwattana et al. \(2017\)](#) employ Gaussian blur on colon histology images for the task of gland segmentation. [Zhang et al. \(2019a\)](#) show that data augmentation by adjusting image quality enables the largest performance gain in MR images, with largest improvement coming from image sharpening through the application of unsharp masking.

By image appearance: Data augmentation by adjusting image appearance consists in manipulating the statistical characteristics of the image intensities such as brightness, saturation and contrast. [Liskowski and Krawiec \(2016\)](#) apply gamma correction of saturation and value of the HSV color space prior to segmenting retinal blood vessels. [Dong et al. \(2017\)](#) employ random enhancement of brightness in 3D MR volumes to enrich the training set for brain tumor segmentation. Contrast augmentation is usually helpful when images exhibit inhomogeneous intensities. For instance, [Fu et al. \(2017\)](#) apply a contrast transformation function on fluorescence microscopy images to enrich the dataset for the task of nuclei segmentation. [Alex et al. \(2017\)](#) use histogram matching as a form of pre-processing where the 3D MR images are matched against an arbitrarily chosen reference image from the training data.

By image layout: Data augmentation by changing image layout consists of spatial transformations such as rotation, scaling and deformation. [Ronneberger et al. \(2015\)](#) show that augmenting the training set with random elastic deformations is key to training a segmentation network with very few annotated images. [Milletari et al. \(2016\)](#) also apply a dense deformation field through a 2x2x2 grid of control-points and B-spline interpolation on the training images. [Çiçek et al. \(2016\)](#) first sample random vectors from a normal distribution in a grid with a spacing of 32 voxels in each direction and then apply a B-spline interpolation.

4.1.2. Mixing Augmentation

Mixup is a data augmentation method wherein new training images and the corresponding labels are generated through a convex combination of pairs of training images and their labels. Mixup was originally proposed for the task of image classification; however, its extension to image segmentation is straightforward. Given two images x_i, x_j and their corresponding masks y_i, y_j , the new image and mask are computed as follows:

$$\tilde{x} = \lambda x_i + (1 - \lambda) x_j$$

$$\tilde{y} = \lambda y_i + (1 - \lambda) y_j$$

where λ is sampled from a beta distribution. Despite its simplicity, mixup has been highly effective for both natural and medical images. [Panfilov et al. \(2019\)](#) report improved generalization of a knee segmentation model when mixup is used for data augmentation. Using a linear combination of existing labels, mixup typically generates soft labels. [Li et al. \(2019c\)](#) propose asymmetric mixup that turn soft labels generated by mixup into hard labels, which, according to their experiments improve the segmentation of brain tumors in various data regimes. The success of mixup at the input data space has further inspired its use in the latent feature space, a technique called manifold mixup [Verma et al. \(2019\)](#). Manifold mixup has recently proved effective for prostate cancer segmentation on MR image [Jung et al. \(2019\)](#), improving Dice by two to four points depending on the neural architecture used for segmentation.

4.1.3. Synthetic Augmentation

Synthetic data augmentation methods for medical image segmentation can be broadly grouped into same-domain and cross-domain image synthesis. The former consists of synthesizing labeled data directly in the target domain. The latter, on the other hand, consists of projecting labeled data from another domain to the target domain, which is closely related to the subject of domain adaptation. We therefore postpone a detailed review of cross-domain image synthesis methods until Section 4.2.2, where we present a detailed study of domain adaptation techniques.

We have summarized the representative approaches of same- and cross-domain image synthesis methods in Table 1. As seen, cross-domain synthesis is based primarily on CycleGAN whereas same-domain synthesis uses various methodologies including CycleGANs, conditional GANs, and transformation networks. In the following, we review the methods suggested for same-domain image synthesis.

Via CycleGANs: Fu et al. (2018a) propose a spatially constrained CycleGAN to generate synthetic 3D microscopy images. The spatial constraints guide the CycleGAN so that the nuclei appear in desired locations and orientations in the synthetic images. The results show that the synthetic images generated by spatially constrained CycleGAN are more effective than CycleGAN in improving the performance of the base segmentation model.

Via conditional GANs: Guibas et al. (2017) propose a framework consisting of a GAN and a conditional GAN to generate pairs of synthetic fundus images and the corresponding vessel masks. Specifically, the GAN takes as input a random vector and then generates a synthesized vessel mask, which is then sent to the conditional GAN to generate the corresponding photo-realistic fundus image. The authors verify the fidelity of the synthesized images by examining whether a classifier can distinguish the synthetic images from the real images, but do not demonstrate whether the synthesized examples enable training a more accurate segmentation model.

Tang et al. (2018) train a stacked GAN (SGAN) to pre-process CT images, where the first GAN generates a denoised image and the second GAN generates a high resolution image. The SGAN was trained on a large external dataset (DIV2K- 1000 images Agustsson and Timofte (2017)). Pre-processing using this method resulted in significantly improved segmentation performance on both deep learning (HNN) and non deep learning (GrabCut) approaches on the DeepLesion dataset Yan et al. (2018). Tang et al. (2019a) propose a 2-stage framework for lung segmentation in chest X-ray (CXR) where a segmentation model is first trained on 280 real images, and then fine-tuned using 5000 synthetic CXR. The authors use a pix2pix network Huang et al. (2018a) for image synthesis, which transforms an image of a healthy CXR into one with pathology. They observe that across different segmentation models, this augmentation significantly increases precision, recall, and Dice score.

Shin et al. (2018) use a conditional GAN to generate synthetic MR images given a lesion mask and a brain

segmentation mask. Once trained, the synthesis network can generate synthesized MR images given a user-defined tumor mask. The elegance of this approach is in how the user can rescale or relocate a tumor in the mask and then the synthesis network can generate the MR image in accordance to the new size and location of the tumor. Without typical data augmentation, the tumor segmentation model trained using both synthetic and real MR images achieves a significant performance gain over the model trained using only real MR images. However, the performance gap is largely bridged in the presence of typical data augmentation.

Tang et al. (2019b) use a mask-guided GAN to augment their lymph node segmentation dataset. For this purpose, the authors use pairs of lymph node images and segmentation masks from 124 patients. The trained GAN then generates 5000 lymph node images, each generated based on a user-provided mask. Augmenting the dataset with 5000 synthesized images significantly improves all performance metrics. In a similar spirit, Mahapatra et al. (2018) use a conditional GAN to synthesize X-ray images with desired abnormalities. The model takes as inputs an X-ray with an abnormality and a lung segmentation mask, and then it generates a synthesized X-ray that has the same diseases as the input X-ray while taking the image appearance that matches the provided segmentation mask. This approach has the capability of generating many synthesized diseased images from one real diseased image. A similar approach is also adopted by Abhishek and Hamarneh (2019) where conditional GAN is trained to generate synthesized skin images from user-defined lesion masks. The authors show that synthesized images, when combined with traditional augmentation, achieve 4 points increase in Dice over the same model trained using only traditional data augmentation.

Lung segmentation is challenging in the presence of large pleural nodules, which are often under-represented in the training sets. To overcome this limitation, Jin et al. (2018) train an image in-painting model based on a conditional GAN that can synthesize pleural nodules in the nodule-free CT slices. The authors test the lung segmentation model using 34 images with peripheral nodules from the LIDC dataset, demonstrating that the model trained with the synthetic data achieves 2 points increase in Dice over the model trained using only real images.

Via transformation networks: Zhao et al. (2019a) propose a data synthesis method to generate pairs of brain MR images and the segmentation masks from only one labeled MR image. For this purpose, the authors suggest a hybrid spatial-intensity transformation model. The spatial transformation network deforms the labeled image so it takes the spatial layout of a given unlabeled image. Once the layout is taken care of, the intensity transformation network changes the intensity at each pixel so the labeled image takes the appearance of a given unlabeled image. Together, the two transformation networks enable the generation of new labeled examples from a reference labeled image and a number of unlabeled images. For the task of brain structure segmentation, the suggested data augmentation method enables four points increase in Dice over

Table 1: Comparison between image synthesis methods suggested for medical image segmentation.

Publication	Synthesis Type	Domains	Description
Chartsias et al. (2017)	Cross-domain synthesis	CT \rightarrow MRI	CycleGAN is used to generate pairs of synthesized MR images from labeled CT slices
Zhang et al. (2018d)	Cross-domain synthesis	CT \leftrightarrow MRI	CycleGAN with shape consistency loss is used to translate between MR and CT scans
Fu et al. (2018a)	Same-domain synthesis	3D Microscopy	CycleGAN with spatially constraints is used to synthesize 3D microscopy images
Guibas et al. (2017)	Same-domain synthesis	Fundus	Conditional GAN and Vanilla are used to generate a vessel mask and the corresponding fundus image
Shin et al. (2018)	Same-domain synthesis	MRI	Conditional GAN to generate synthetic MR images given a lesion mask and a brain segmentation mask
Jin et al. (2018)	Same-domain synthesis	CT	Conditional GAN is used to synthesize pleural nodules in the nodule-free CT slices
Tang et al. (2018)	Same-domain synthesis	CT	Conditional GAN is used to synthesize higher contrast preprocessed images
Tang et al. (2019b)	Same-domain synthesis	CT	Conditional GAN is used to synthesize CT lymph node images given lymph node mask
Tang et al. (2019a)	Same-domain synthesis	X-ray	Conditional GAN is used to synthesize X-ray images with desired abnormalities
Mahapatra et al. (2018)	Same-domain synthesis	X-ray	Conditional GAN is used to synthesize X-ray images with desired abnormalities
Abhishek and Hamarneh (2019)	Same-domain synthesis	Skin images	Conditional GAN is used to synthesize skin images from user-defined lesion masks
Zhao et al. (2019a)	Same-domain synthesis	MRI	Hybrid spatial-intensity transformation network is used to synthesize MR images
Chaitanya et al. (2019)	Same-domain synthesis	MRI	Hybrid spatial-intensity transformation network is used to synthesize task-driven MR images
Xu and Niethammer (2019)	Same-domain synthesis	MRI	Spatial transformation network is used to synthesize task-driven MR images

a model trained using traditional data augmentation and 3 points increase in Dice over atlas-based data augmentation. Noteworthy, the suggested method is tested in a 1-shot medical image segmentation setting, where only one labeled example is available for training. It is not clear whether the performance gain holds up in the presence of larger labeled training sets.

Concurrent to the work above, Chaitanya et al. (2019) propose a few-shot image segmentation model based on a task-driven data augmentation method, wherein an intensity and a deformation network generate synthetic pairs of image-mask to enrich the training set. The two transformation networks are conditional generators, which are trained in an adversarial manner so that the transformed images resemble the appearance of labeled and unlabeled images in the dataset. Also, to ensure that the synthetic images are relevant to the target task (segmentation), the transformation networks are trained jointly with the segmentation network by feeding the synthetic images to the segmentation network. The authors test the model for cardiac segmentation in MR images from 20 subjects, demonstrating marked improvement in Dice when only 1 or 3 labeled images are used for training. The authors report even larger improvement when they combine their synthetic images with mixup Zhang et al. (2018a).

4.1.4. Summary

In this section, we first reviewed the traditional data augmentation methods, which manipulate image appearance, quality, or layout to generate new training examples. Although simple to implement, these methods result in augmented images that are typically correlated with the original images; and thus, their impact may be limited. We then reviewed data augmentation methods that generate new images and masks through linear combination of existing labeled images. We also reviewed data augmentation methods based on image synthesis, which generate images with larger appearance variability than those generated by the traditional data augmentation. Image synthesis methods achieve this by sampling from the manifold on which the original training set reside. Although these methods are more effective for handling data scarcity as well as rare conditions, they are more demanding to implement, because their training schemes typically require adversarial networks and additional labeled or unlabeled datasets.

4.2. Leveraging External Labeled Datasets

The problem of scarce annotations can be alleviated by employing external labeled datasets via transfer learning, domain adaptation or dataset fusion techniques. Transfer learning typically involves model pre-training, wherein a large external labeled dataset is used to train an initial model, which can then be fine-tuned using the target dataset. Domain adaptation techniques attempt to bridge the distribution gap between the different datasets by either learning a common latent representation or by learning to translate images from one domain to the other. Dataset fusion, on the other hand, simply utilizes data from one or multiple external datasets to train a general segmentation model having superior performance to those trained on each individual dataset. We have compared the inference stage of the aforementioned methodologies in Figure 2 where architecture details such as skip connections and dense blocks are not shown for the sake of grouping the overarching ideas together. We have further listed the representative works of the above methodologies in Table 2.

4.2.1. Transfer Learning

When dealing with small medical image datasets it is possible to leverage the power of non-medical image data as well. Transfer learning from natural images has been widely adopted for medical image classification Tajbakhsh et al. (2016); Shin et al. (2016); however the application to medical image segmentation has been scarce. This trend is in part due to the 3D nature of medical images, which hampers transfer learning from 2D models trained on natural images, and also partially due to the promising performance of shallower segmentation networks in medical imaging, which unlike deep models may not benefit from fine-tuning. Nevertheless, we briefly describe the two common scenarios for transfer learning in medical imaging and then introduce the works that enable transfer learning from 2D models to 3D medical applications.

2D \rightarrow 2D: There are two main approaches to transfer knowledge from natural images to 2D medical image segmentation models. The first approach (e.g., Ma et al. (2019)) is to fine-tune an autoencoder that is pre-trained for the task of image segmentation in natural images. The advantage of this approach is that both encoder and decoder are pre-trained, but

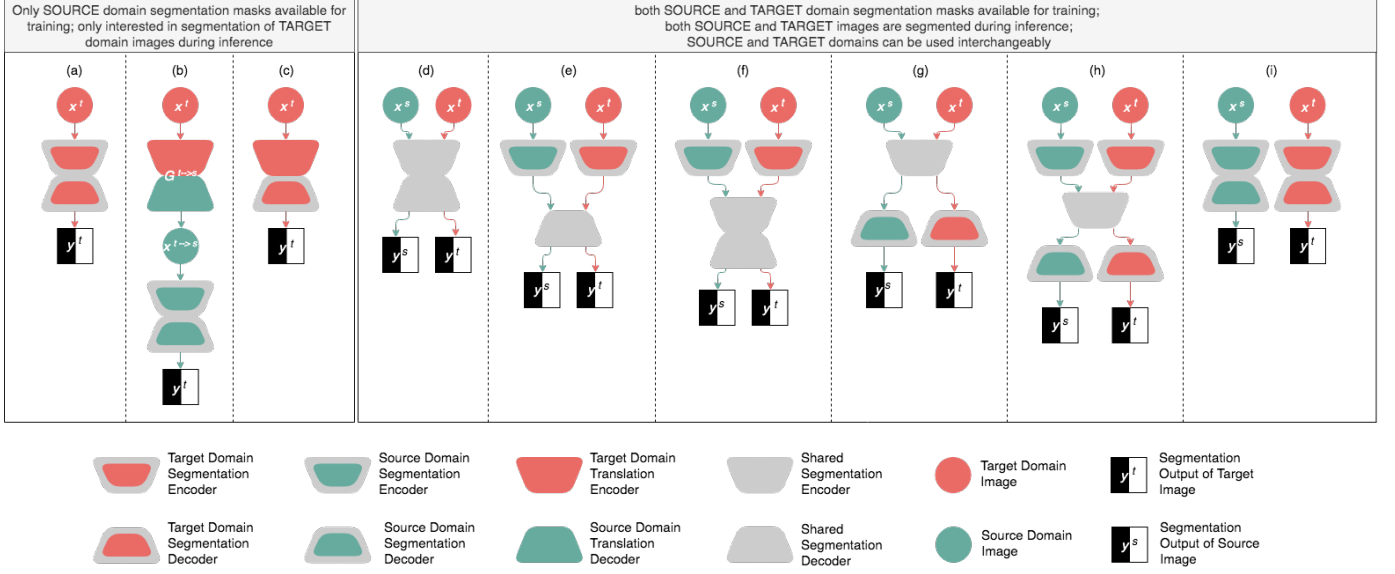


Figure 2: Leveraging external labeled datasets is effective for the problem of scarce annotations. This figure compares the data flow during inference for the related solutions: (a)-(c) cover approaches that only use source domain labels during training while (d)-(i) cover approaches that make use of both source and target domain labels, in which case the terms ‘source’ and ‘target’ are no longer meaningful and can be used interchangeably. (a) Target domain images are directly passed through the segmentation network trained on images from the target domain and images translated to the target domain. (b) Target domain images are converted to the source domain and then sent to the segmentation network trained on the source domain and source-like images. (c) Target domain images are sent through the target domain encoder (belonging to the domain translation network) and then sent to the segmentation decoder trained on target domain and target-like images. (d) Images from either domain can be passed through the segmentation network trained jointly on both domains. (e) Both domain images are passed through their own domain specific encoders and then through the segmentation decoder trained on both domains. (f) Similar to (e) but now the domain specific encoded feature maps are sent through a jointly trained segmentation encoder and decoder, (g) Images from both domains pass through a jointly trained segmentation encoder and then pass through domain specific decoders, (h) Each domain has its own specific encoder and segmentation decoder, but pass through a shared segmentation encoder in between. (i) Each domain has its own segmentation network during inference which is trained using data from its own domain augmented using domain translation.

the disadvantage is that natural image segmentation datasets are not massive. The second approach (e.g., [Qin \(2019\)](#)) is to append a randomly initialized decoder to an encoder pre-trained for the task of image classification in natural images, followed by fine-tuning the entire network. This approach has the advantage of knowledge transfer from a massive natural image classification dataset, but the disadvantage is that the decoder needs to be initialized from scratch.

2D \rightarrow 3D: The aforementioned approaches, while effective, are applicable to only 2D medical image segmentation. Knowledge transfer from 2D models pre-trained on natural images to the models targeted at 3D medical applications has been a little explored topic. [Yu et al. \(2018\)](#) transfer models based on natural scene video by treating the third dimension of medical scans as a temporal axis. This approach however may fail to capture the 3D context of medical scans. [Liu et al. \(2018\)](#) propose to turn a 2D model into a 3D network by extending 2D convolution filters into 3D separable anisotropic filters. With this approach, one can use 2D models to initialize 3D models for target medical image segmentation applications.

4.2.2. Domain Adaptation

A frequently encountered obstacle in medical imaging is that of a distribution shift between the data available for training and the data encountered in clinical practice. This shift could be caused by using different scanners and image acquisition protocols or due to imaging different patient populations

and ethnicities. As individual datasets tend to be small and typically originate from a single institution, they are inherently biased and the resulting models tend to perform poorly in the real world. Given the limitations of individual datasets, a natural workaround is to incorporate multiple datasets for training. Domain adaptation techniques attempt to bridge the gap between multiple domains by either learning a latent representation that is common to these various domains or by learning to translate images from one domain to the other. These domains may consist of different imaging modalities or different image distributions within the same modality.

A recurring theme in many of the domain adaptation papers discussed in this section is the use of GANs, CycleGANs, or some sort of adversarial loss for the purpose of image reconstruction. Therefore, we first briefly explain these methods and then cover their applications to medical image segmentation. GANs by [Goodfellow et al. \(2014\)](#) make use of dual networks: a generator and discriminator, which are trained to compete against each other. The discriminator is trained to distinguish between real and synthetic images and the generator is trained to synthesize realistic images that the discriminator cannot distinguish from the real images. When this is used in the context of domain translation, the generator learns a mapping from one domain to another. CycleGANs by [Zhu et al. \(2017\)](#) achieve this by using two pairs of generators, each with its own discriminator, one to map from the source to the target domain and the other for the inverse mapping. In addition to

Table 2: Overview of the papers leveraging external labeled datasets. The suggested method, among other factors, differ in terms of presence of target domain labels and the domain in which segmentation is performed. The Figure column on the right shows the matching data flow from Figure 2.

Publication	Availability of Target Domain Segmentation Masks	Segmentation Domain	Modality	Figure
Transfer Learning				
Ma et al. (2019)	✓	Target	2D→2D	(a)
Qin (2019)	✓	Target	2D→2D	(a)
Liu et al. (2018)	✓	Target	2D→3D	(a)
Yu et al. (2018)	✓	Target	2D→3D	(a)
Domain Adaptation				
Huo et al. (2018a)	✗	Target	MRI, CT	(a)
Huo et al. (2018b)	✗	Target	MRI, CT	(a)
Chen et al. (2019b)	✗	Target	bSSFP, LGE	(a)
Chen et al. (2018)	✗	Source	X-ray	(b)
Zhang et al. (2018c)	✗	Source	DRR, X-ray	(b)
Chen et al. (2019a)	✗	Target	MRI, CT	(c)
Giger (2018)	✗	Source	MRI, CT	(b)
Chartsias et al. (2017)	✓	Both	MRI, CT	(i)
Zhang et al. (2018d)	✓	Both	MRI, CT	(i)
Dou et al. (2018)	✓	Both	MRI, CT	(e)
Valindria et al. (2018)	✓	Both	MRI, CT	(d),(e),(f),(g),(h)
Dataset Fusion				
Harouni et al. (2018a)	✓	All domains	MRI,CT,US,X-ray	(d)
Dmitriev and Kaufman (2019)	✓	All domains	CT	(d)

the adversarial loss a cycle consistency loss ensures that the result of the mapping followed by the inverse mapping is identical to the input. Multimodal unsupervised image-to-image translation (MUNIT) Huang et al. (2018a) differs from CycleGAN in that the generators, that translate between the domains, are each composed of an encoder that explicitly disentangles the domain-invariant structure of the images from their domain-specific style before passing both to the decoders. While CycleGAN provides a one-is-to-one mapping between the two domains, MUNIT allows a one-is-to-many mapping by sampling from the style encoding distribution.

Domain Adaptation without Target Labels: When the test domain (a.k.a the target domain) labels are unavailable, but we only have access to labels from a different domain (a.k.a the source domain), the popular approach is to convert one domain to the other.

Source → Target: In the absence of target labels, one approach is to convert the source domain images to have the style of the target domain while retaining the anatomical structure and thereby the segmentation masks of the source domain. Then, a segmentation network trained on the target-styled images and source masks can be used to make predictions on the target images. Huo et al. (2018a) suggest a joint image synthesis and segmentation framework that enables image segmentation for the target domain using unlabeled target images and labeled images from a source domain. The intuition behind this joint optimization is that the training process can benefit from the complementary information between the synthesis and segmentation networks. In this framework, the main job is done by the image synthesis network, a CycleGAN, that

converts the labeled source images to synthesized target images. The synthesized target images are used to train the segmentation network. At test time, the real images from the target domain are directly submitted to the segmentation network to obtain the desired segmentation masks. The authors evaluate this framework for the task of spleen segmentation in CT scans where the 19 target abdominal CT scans do not have the segmentation masks, but the 60 source abdominal MR images come with spleen masks. Experimental results show that the model trained (leave-one-out cross validation using 19 CT scans) using synthesized CT scans can achieve a performance level at par to the model trained using real CT scans with labels. The authors further extend their work in Huo et al. (2018b) for the task of splenomegaly and total intracranial volume segmentation, reporting 2% improvement in Dice over the existing state of the art—a 2-stage CycleGAN followed by a separate segmentation network. For the task of total intracranial volume segmentation, the Dice coefficient using domain adaptation is only 1% lower than the Dice coefficient of the model trained with the target labels (upper bound).

Chen et al. (2019a) perform domain translation from the MR to CT domain for the task of heart CT segmentation using only MR image masks. They propose the use of a CycleGAN for conversion from MR to CT and vice-versa (20 volumes each with a 80-20 training-testing percentage split) with a segmentation network trained on the real and generated CT (target) images. The novelty of their approach lies in the use of a shared encoder common to both the CT segmentation network and the CT to MR generator network, which makes use of this multitask setting to prevent the segmentation

encoder from over-fitting. The authors report a 9% improvement in Dice over the existing state of the art domain adaptation techniques.

Chen et al. (2019b) makes use of MUNIT to translate between balanced steady-state free precession (bSSFP) images having masks for 3 cardiac structures and late-gadolinium enhanced (LGE) images that don't have any masks. The framework is trained and evaluated on the multi-sequence cardiac MR segmentation challenge (MS-CMRSeg 2019) dataset. The translation network is trained with 40 images from each domain and this is used to create a synthetic dataset of 150 target domain LGE images from 30 bSSFP images (sampled 5 times from the style encoding distribution). The synthetic LGE images with the original bSSFP masks are then used to train the segmentation network. The authors evaluate their approach on the five validation images provided by the challenge and show a 10% increase in Dice compared to a registration-based approach.

Target \rightarrow Source: Alternatively, one can convert the target domain images into the source domain followed by training the segmentation model using the source images. During inference, the target images are first converted to the source domain and then fed to the segmentation network to generate the segmentation maps.

Giger (2018) propose converting the CT (target) domain to the MR (source) domain and then using an existing atlas-based algorithm (MALP-EM) to perform the segmentation on the converted MR images. The motivation is that it is easier to obtain segmentation annotations for brain MRI than brain CT scans. They use a modified U-Net for the domain conversion, which requires the 10 pairs of CT and MR images to be registered beforehand and then perform multi-modal registration using 15 atlases. On average, they improve the Dice score by 9% over a baseline that performs segmentation in the CT domain.

Chen et al. (2018) use the CycleGAN with an additional semantic adversarial loss, which is used to distinguish between source segmentation masks and segmentation predictions of the converted target to source images. The authors evaluate their proposed method on 2 different X-ray datasets, which vary in disease type, intensity, and contrast (source: Montgomery set with 138 cases; target: JSRT set with 247 cases; 70-10-20% training-validation-testing split). They achieve 2% improvement in Dice over the baseline CycleGAN performance.

Given a set of annotated CT scans, Zhang et al. (2018c) aim to segment X-ray images without having any X-ray segmentation annotations. For this purpose, the authors first convert annotated CT scans to digitally reconstructed radiographs (DRRs) via a 3D to 2D projection, and then learn a mapping between 815 DRRs and 73 training X-ray images. The mapping is performed by a task-driven GAN, which is a CycleGAN with an additional segmentation loss to generate segmentation masks for the DRR-style images. With these new constraints, tested on 60 X-ray images, the suggested method improves the segmentation Dice by two or three points over

using either one of them alone and over the vanilla CycleGAN.

Domain Adaptation with Target Labels: If the segmentation masks are available for both domains, there is no longer a distinction between the choice of source and target domains. In this scenario, domain adaptation is achieved by learning a shared feature encoding, allowing the segmentation network to predict meaningful masks regardless of the input domain.

Chartsias et al. (2017) use CycleGAN to generate pairs of synthesized MR images and the corresponding myocardium masks from pairs of CT slices and their myocardium segmentation masks. The authors base the image synthesis module on CycleGAN, because it does not require the 15 training CT and 15 training MR images to be registered nor do they have to belong to the same patient. Once the synthetic data is generated, the authors train a myocardium segmentation model using both synthetic MR and real MR images, demonstrating 10% improvement over the myocardium segmentation model trained using only the real MR images, when tested on 5 MR images.

However, Zhang et al. (2018d) demonstrate that the above offline data augmentation may only be partially effective and in some cases can even deteriorate the performance. Instead, they propose a framework wherein both data synthesis model and segmentation model are trained jointly. They develop a segmentation network that can segment heart chambers in both CT and MR images by learning a translation between the two domains. They use a CycleGAN as their backbone and further add a shape consistency loss to ensure anatomical structure invariance during translation. Their dataset makes use of 142 CT volumes to match the number of MRI volumes. For both modalities, 50% data is used as training and validation, and the remaining 50% as testing data. They improve the Dice score on CT images by eight points and MR images by two points over other methods that use both real and synthetic data for training.

Dou et al. (2018) train a cardiac segmentation network, consisting of two parallel domain-specific encoders and a shared decoder. During training, the decoder takes its input from a single encoder depending on the domain of the input image. The network is trained so that the decoder yields similar high-level semantic embedding for images of both domains. This is achieved by a discriminator that is trained to distinguish between the two domains. The authors use the challenge dataset by Zhuang et al. (2019), which contains 20 subjects with MR images and masks, and an additional 20 non-overlapping subjects with CT images and masks. Using 16 subjects from each modality for training and 4 for testing, they achieve substantial performance boost over single domain training and 2% improvement in Dice over other domain adaptation techniques.

For the case where both source and target labels are available, domain adaptation is achieved using shared latent representations between the two domains, but the location of the shared features is a network design choice. Valindria et al. (2018) evaluate the performance of four different locations for the shared latent representations: 1) separate encoders with a shared decoder (see Figure 2(e)), 2) separate initial streams,

followed by a shared encoder and decoder (see Figure 2(f)), 3) shared encoder and separate decoder streams (see Figure 2(g)) and finally, 4) separate encoder and decoder streams with a shared latent representation in-between (see Figure 2(h)). They compared these variants with a baseline consisting of a single-stream encoder-decoder segmentation network, which is trained with data from both domains (see Figure 2(d)). The authors perform 2-fold cross-validation based on 34 subjects for MRI and 30 subjects for CT. Their results showed that the baseline was actually at par with or in some cases outperformed most variants, the only exception being the fourth variant, which consistently outperformed the baseline and other dual stream variants.

4.2.3. Dataset Fusion

Dataset fusion techniques leverage multiple datasets to train a universal segmentation model based on heterogeneous, disjoint datasets, offering two advantages: 1) more efficient training, as multiple models are consolidated into a single model, and 2) enhanced regularization, as data from multiple sources can provide further supervision. Domain adaptation and Dataset fusion both aim to leverage multiple datasets; however, they take different approaches: the former does this by minimizing the domain shift, whereas the latter does so by learning to discriminate between domains.

It is inefficient to have modality-specific models to segment the same organs across different modalities. Harouni et al. (2018a) propose a modality independent model that is jointly trained using data from all modalities. The network architecture is a modified U-Net with the base U-Net performing multi-organ segmentation and a classification head added to the bottleneck layer, which performs the modality/viewpoint classification (7 classes: X-ray, short axis MRI, 2-chamber MRI, 4-chamber MRI, CT, ultrasound 4-chamber B-mode, Doppler ultrasound). The authors compared their jointly trained universal network against individually trained U-Nets for each task, using data from multiple sources split at the patient-level such that 65% (2781 2d images) was used for training and the remaining 35% (1016 2d images) for validation. The results show that the universal network usually performed at par with or outperformed the specialized networks. The exception to this performance was seen for left ventricle segmentation, where a dedicated MRI model showed significantly higher performance.

Dmitriev and Kaufman (2019) train a multi-organ segmentation model using data from multiple single organ datasets. For this purpose, the authors add an additional channel, which is filled with a class-specific hash value, to each layer of the decoder network, conditioning the segmentation predictions on the class labels. The drawback, however, is that the test image with an unknown organ label must be fed in ‘m’ times sequentially to condition on all the possible classes. The authors use 20 volumes with liver masks from the publicly available Sliver07 dataset, 82 volumes with pancreas masks from the publicly available NIH pancreas dataset, and 74 volumes of their own additional dataset of liver and spleen segmentation wherein each dataset was divided into

training and testing sets with an 80/20 ratio. The multi-dataset training scheme achieves 1.5% improvement in Dice over the state of the art single dataset approaches.

4.2.4. Summary

In this section, we reviewed techniques that utilize additional labeled datasets to enhance the segmentation performance over the counterpart models trained using data from a single domain. These methods fell into three distinct categories: (1) transfer learning (Section 4.2.1); 2) domain adaptation with and without target annotations (Section 4.2.2), where the former is used to translate in the absence of target domain annotations whereas the latter learns a shared feature representation between the two domains, and (3) dataset fusion (Section 4.2.3), which learns to discriminate between the domains in order to condition the segmentation based on the domain of the input image. In general, the models trained with target domain annotations are bound to generalize better to the target domain; however, the appealing feature of domain adaptation methods without target annotations is independence from the target domain annotations, which makes these methods the only viable solution to deal with unlabeled target domain images. The majority of domain adaptation techniques require some form of adversarial training, making them tricky to train. On the other hand, transfer learning and dataset fusion require minimal changes to the network architecture, allowing for simple and successful joint dataset training.

4.3. Cost-effective Annotation

Perhaps, the most reliable approach to the scarce annotation problem is to obtain additional labeled examples. This approach requires the availability of unlabeled medical images, access to a pool of expert annotators, and more importantly additional annotation budget. However, to fully utilize the annotation budget, one must decide how to choose examples for annotation from a large set of unlabeled images and how to accelerate the annotation process given the limited availability of medical experts. The former question is addressed by active learning, which determines the next batch of samples for annotation so as to maximize model’s performance, and the latter is addressed by interactive segmentation, which assists the expert annotators by propagating their modifications through the entire segmentation mask.

4.3.1. Active Learning

Active learning is a cost-effective approach to enlarge the training datasets; and thus, it is highly amenable to the problem of limited annotation budget in medical image segmentation where clinical experts have limited availability, annotation cost is high, and the amount of unlabelled data is usually non-trivial. Active learning, in its general form, requires the availability of a base segmentation model; thus, a minimal set of base annotations is necessary. Therefore, datasets with no segmentation masks or those with only weak annotations may not directly benefit from active learning unless a pre-trained model from a similar domain is available

Publication	Query mode	Sample selection strategy			Annotation unit
		Informativeness	Diversity	Annotation cost	
Gorriz et al. (2017)	Iterative	✓			Whole 2D image
Yang et al. (2017)	Iterative	✓	✓		Whole 2D image
Ozdemir et al. (2018)	Iterative	✓	✓		Whole 2D image
Kuo et al. (2018)	Iterative	✓	✓	✓	Whole 3D image
Sourati et al. (2018)	Iterative	✓	✓		2D image patch
Mahapatra et al. (2018)	One-shot	✓			Whole 2D image
Sourati et al. (2019)	Iterative	✓	✓		2D Image patch
Zheng et al. (2019)	One-shot		✓		2D Image patch

Table 3: Comparison between active learning methods for medical image segmentation. The suggested methods differ in terms of the definition of the annotation unit and the criteria by which these units are selected for the next round of annotation.

Algorithm 1: Active learning

Input : Initial model \mathcal{M}_0 , unlabeled dataset \mathcal{U}_0 , size of query batch k , iteration times \mathcal{T} , active learning algorithm \mathcal{A}

Output: Labeled dataset $\mathcal{L}_{\mathcal{T}}$, updated model $\mathcal{M}_{\mathcal{T}}$

```

1  $\mathcal{L}_0 \leftarrow \emptyset$ ;
2 for  $i \leftarrow 1$  to  $\mathcal{T}$  do
    /* phase 1: query batch selection */
3    $\mathcal{Q}_i \leftarrow \mathcal{A}(\mathcal{U}_{i-1}, \mathcal{M}_{i-1}, k)$ ;
4   annotate samples in  $\mathcal{Q}_i$ ;
    /* phase 2: update model */
5    $\mathcal{L}_i \leftarrow \mathcal{L}_{i-1} \cup \{(\mathbf{x}, y) | \mathbf{x} \in \mathcal{Q}_i, y \in \mathcal{Y}_i\}$ ;
6    $\mathcal{M}_i \leftarrow \text{fine-tuning } \mathcal{M}_{i-1} \text{ using } \mathcal{L}_i$ ;
7    $\mathcal{U}_i \leftarrow \mathcal{U}_{i-1} \setminus \mathcal{Q}_i$ ;
8 end
9 return  $\mathcal{L}_{\mathcal{T}}, \mathcal{M}_{\mathcal{T}}$ 

```

to serve as the base segmentation model. In what follows, we present a high-level overview of the active learning paradigm and then review the active learning methods for medical image segmentation.

Active learning is an iterative paradigm wherein the unlabeled samples for each round of annotation are selected judiciously to maximally improve the performance of the current model. Algorithm 1 shows the pseudocode of active learning. In each iteration, the segmentation model is run against the unlabeled images, and then a set of selection criteria, which are defined on model outputs, are used to select the next batch of samples for annotation. Once annotated, the new batch is added to the training set and the segmentation model is fine-tuned using the augmented training set. This process is repeated until the performance on a validation set plateaus. Active learning methods differ in their sample selection criteria and their definition of annotation unit (the whole or only a part of the image is to be annotated). Table 3 compares the active learning methods suggested for medical image segmentation.

Yang et al. (2017) propose a framework called suggestive annotation where the candidate samples for each round of annotation are selected through a 2-stage screening process.

First, uncertain samples are identified through the application of an ensemble of segmentation models. The uncertainty at pixel-level is computed as the variance of predictions generated by individual models in the ensemble. Pixel level uncertainty is then averaged to form one uncertainty value for the entire image. Second, the uncertain images are further refined by removing the samples that have high visual similarity. The authors evaluate suggestive annotation on a histopathology dataset for gland segmentation (85 training and 80 test images) and a CT dataset for lymph node segmentation (37 training and 37 test images), achieving the full-dataset performance with only 50% of training data.

Kuo et al. (2018) propose an active learning framework based on sample uncertainty and annotation cost. In fact, this work is the first of its kind in the context of medical image segmentation to account for annotation cost when selecting the samples for the next round of annotation. Without considering annotation cost, active learning frameworks treat the images equally, ignoring the fact that some images in practice incur substantially higher annotation cost due to the larger size or quantity of contained target structures (organs and abnormalities). Concretely, they formulate active learning as a knapsack 0-1 problem where the objective is to select a batch of samples for annotation so as to maximize the model uncertainty while keeping the annotation cost below a given threshold. To measure sample uncertainty, they propose to train FCNs at the patch-level rather than the image-level because a patchFCN is less likely to overfit to the global image context. To estimate annotation cost for each unlabeled image, they use a regression model where the predictor variables are the total perimeter and number of connected components in the segmentation mask. The authors evaluate the suggested active learning method for intracranial hemorrhage segmentation on 1247 head CT scans (934 training/313 test), achieving the performance of a full-dataset model with 50% of the training set and 20% of annotation cost. These results are comparable to Yang et al. (2017), but are obtained using datasets that are two orders of magnitude larger in size.

The methods suggested by Kuo et al. (2018); Yang et al. (2017), despite their differences, both employ an ensemble of FCNs to estimate sample uncertainty, which is slow and computationally expensive to train, as one needs to iteratively

train an ensemble of segmentation models after each round of annotation. A more computationally efficient approach to quantifying model uncertainty is to run a given sample through the model several times with the dropout layers on [Gal and Ghahramani \(2016\)](#). Pixel uncertainty is then estimated as the entropy of averaged probabilities over different classes. This efficient sample uncertainty estimation is used by [Gorriz et al. \(2017\)](#) to realize a cost-effective active learning framework. Specifically, they compute an uncertainty value for a given unlabelled image by first obtaining an uncertainty map using the aforementioned dropout-based method followed by reducing the map to a single value through a weighted averaging scheme where the weights come from a distance transform map over the segmentation result. The idea is to assign higher importance to the uncertain pixels that are located farther away from the object boundaries. Once uncertainty values are computed for all unlabelled images, at each round of active learning, they select samples with high uncertainties as well as a batch of random samples for annotation. In each round, they also directly add samples that have the lowest levels of uncertainty along with their predicted masks to the training set. The rationale is that if the sample uncertainty is low, then the model has probably created a high-quality segmentation mask, which can be used for training without any further corrections. The authors evaluate this approach for melanoma segmentation in ISIC 2017 challenge dataset for Skin Lesion Analysis (1600 training and 400 test images), demonstrating a 55% reduction in the annotation cost.

Similar to [Yang et al. \(2017\)](#), [Ozdemir et al. \(2018\)](#) propose a 2-stage active learning framework where stage 1 identifies uncertain examples whereas stage 2 selects the representative examples among the uncertain examples. The suggested method is however different in how uncertainty and representativeness are measured. The authors use the dropout-based approach [Gal and Ghahramani \(2016\)](#) to estimate an uncertainty map for each unlabelled image. To identify representative examples, they use the latent space learned by the segmentation network; however, to increase the discrimination power of the latent space, they train the segmentation network using an entropy-based regularization technique, which encourages diversity among the features of the latent space. The farther an uncertain sample is located from other examples in the latent space, the more representative the example. The uncertainty and representativeness metrics are further fused using Borda count. The authors evaluate their method for muscle and bone segmentation in MR images of 36 patients diagnosed with rotator cuff tear (25 training and 11 test). By ranking the examples using the fused metric metrics, the authors achieve similar performance to the model trained with the full dataset while using only 27% of the entire training set.

[Sourati et al. \(2018\)](#) propose a probabilistic active learning framework where the probability of an unlabeled sample being queried in the next round of annotation is estimated based on its Fisher information. A sample has higher Fisher information if it generates larger gradients with respect to the model parameters. To incorporate Fisher information in the sample

selection process, the authors formulate active learning as an optimization problem where the unknowns are the probabilities by which unlabelled samples are queried for the next round of annotation; the constraints are that the querying probabilities should add up to one and that they should change disproportionately to their Fisher information; and the objective is to assign the querying probabilities so as to maximize the overall Fisher information. The optimization problem above is solved for a batch of samples, as such, the sample inter-dependency is already taken into consideration, eliminating the need for a secondary stage that further selects the representative samples from the informative samples. This one-shot behaviour sets this approach apart from the previous works where informativeness and representativeness are accounted for sequentially (e.g., [Yang et al. \(2017\)](#)). One limitation of this work, however, is that computational complexity is super quadratic with respect to the number of parameters, because the Fisher matrix has as many rows and columns as the number of parameters in the network. This limitation has been addressed in a follow-up work from the authors ([Sourati et al. \(2019\)](#)) where the number of rows and columns of the Fisher matrix reduces to the number of layers in the network. This scheme was tested for brain extraction from MR images of 25 normal newborns and 26 subjects with tuberous sclerosis complex aged younger than 2.5 years old. When trained with only 0.5% of the training voxels, this scheme achieves the same performance as the model that is trained using the entire training set.

[Mahapatra et al. \(2018\)](#) use a Bayesian neural network for active learning where the informative samples are selected using a combined metric based on aleatoric uncertainty (noise in the data) and epistemic uncertainty (uncertainty over the CNN parameters). Thus, this sample selection strategy differs from the previous approaches, where user-defined heuristics such as standard deviation of predictions are used to identify informative samples for annotation. This scheme was evaluated for the segmentation of the clavicles, lungs and heart on chest X-ray images. For this purpose, the authors use training and test sets consisting of 247 and 400 images, respectively. Combined with an image synthesis network, the suggested method achieves the full-data performance with only 30-35% of annotated pixels.

Different from the previous works, [Zheng et al. \(2019\)](#) propose a 1-shot active learning method, which eliminates the need for iterative sample selection and annotation. The suggested method consists of a feature extraction network, which projects each image patch to a latent space, and a clustering algorithm, which discovers representative images for image annotation in the latent space. Being a 1-shot active learning approach, the feature extraction network must be trained using unlabeled data. For this purpose, the authors use various unsupervised models such as auto-encoders and variational auto-encoders. For clustering, the authors use a hybrid method based on K-means and max-cover algorithms. This method was evaluated using a fungus dataset (4 training and 80 test images), a histopathology dataset (84/80), and an MR dataset (10/10). The results for both 2D and 3D datasets

Algorithm 2: Interactive segmentation

Input : Initial model \mathcal{M}_0 , unlabeled image \mathcal{I} , number of iterations \mathcal{N} , feedback operation \mathcal{R} , conversion operation \mathcal{C}

Output: Updated model $\mathcal{M}_{\mathcal{N}}$

```
1 for  $i \leftarrow 1$  to  $\mathcal{N}$  do
  /* generate segmentation map */
2   $\mathcal{S}_i \leftarrow \mathcal{M}_{i-1}(\mathcal{I});$ 
  /* get feedback from an expert */
3   $\mathcal{F}_i \leftarrow \mathcal{R}(\mathcal{S}_i, \mathcal{I});$ 
  /* convert to a new annotation */
4   $\mathcal{A}_i \leftarrow \mathcal{C}(\mathcal{F}_i);$ 
5   $\mathcal{M}_i \leftarrow$  fine-tuning  $\mathcal{M}_{i-1}$  with  $\mathcal{A}_i$ ;
6 end
7 return  $\mathcal{S}_{\mathcal{N}}$ 
```

suggest that the 1-shot active learning method performs comparably to an iterative alternative by Yang et al. (2017).

4.3.2. Interactive Segmentation

Creating segmentation masks is not only tedious and time-consuming for expert annotators, but also incurs substantial annotation cost particularly for volumetric medical images where the same lesion or organ must be delineated across multiple slices. Interactive segmentation can accelerate the annotation process by allowing the expert annotators to interactively correct an initial segmentation mask generated by a model. Interactive segmentation complements active learning in achieving cost-effective annotation: the latter identifies which images to be annotated whereas the former reduces the time required to complete the annotation of a selected image.

Algorithm 2 shows the pseudocode for interactive segmentation. As seen, interactive segmentation may require an initial segmentation model, whose output is reviewed by human experts to provide feedback on possible segmentation error. The user feedback, as the core part of interactive segmentation methodologies, can take varying forms of interactions such as mouse clicks, bounding boxes, and scribbles. The user interactions then translate to foreground or background annotations, which the initial segmentation model can use to improve itself. The updated model re-generates the segmentation mask for the users' feedback, and this process repeats until the desired segmentation mask is obtained. Interactive segmentation is highly effective to cope with a model's inevitable segmentation mistakes, which are typically caused by domain shifts or unrepresentative training sets. In what follows, we summarize the recent interactive segmentation methods that are suggested for medical image segmentation.

Sun et al. (2018a) propose an interactive method for segmenting fuzzy boundaries, wherein the user first places a point roughly at the center of the object, and then the model performs object delineation for the user-specified structure. For accurate boundary segmentation, the authors suggest a segmentation model that delineates the structures by comparing the appearances of image patches from inside and outside of

the structure, imitating inside-outside comparison that physicians perform in order to precisely localize boundaries. The authors model the inside-outside comparison with a **bidirectional convolutional recurrent neural network**, which is trained using the image patch and ground truth mask sequences bidirectionally, allowing the network to learn appearance changes from foreground to background and vice versa. This method, however, only allows users to specify a seed point at the onset of segmentation, that is, the resulting segmentation masks are **not responsive to the subsequent user interaction**.

Wang et al. (2018b) proposes a framework consisting of a proposal network and a refinement network where the former generates a base segmentation mask whereas the latter refines the base mask according to the suggestions provided by the user. **However, the suggested framework lacks adaptability to unseen image contexts.** The authors have overcome this limitation in their followup work Wang et al. (2018a). Given a test image and a pre-trained segmentation model, the suggested framework alternates between 2 steps: 1) refining the current segmentation mask through the application of Graph Cut Boykov and Jolly (2001), and 2) minimizing segmentation loss for the test image by creating a pseudo ground truth segmentation mask. This approach can be viewed as a self-learning method with the difference being the pseudo ground truth depends on both model predictions and user-provided scribbles. Specifically, the pseudo ground truth mask is the predicted segmentation mask wherein the labels of the scribble pixels are overwritten by the labels provided by the user. The segmentation loss is then a weighted cross entropy function, which receives large contributions from the scribble pixels and zero contributions from uncertain pixels. The authors treat a pixel as uncertain if it is located near a scribble but has a predicted label other than that of the scribble or if the posterior distribution predicted by the model has high entropy (low confidence predictions). The suggested framework is evaluated in two applications: brain tumor segmentation using the BraTS dataset Menze et al. (2014) (249 training and 25 test MR images) and multi-organ segmentation in fetal brain MR images (10/8). The results show that the suggested interactive segmentation method outperforms traditional interactive segmentation methods in both accuracy and speed of annotation.

Sakinis et al. (2019) propose a semi-automated image segmentation method that enables a high quality segmentation with only a few user clicks. The authors choose a mouse click as the means of user interaction because it enables quick feedback and ease of simulation. The segmentation model is a U-Net that receives as input the image stacked with the foreground and background attention maps, where attention maps are constructed by placing a Gaussian blob at each foreground and background user click. The U-Net is then trained by minimizing the Dice loss between the predicted segmentation and ground truth. Since it is unfeasible to have true user interaction during training and large-scale testing, the authors propose a simulation scheme that has the effect of a hypothetical user clicking on regions with larger and more noticeable segmentation error. This method proves effective in

segmenting both structures that exist in the training set and the structures that the model has never seen during training. To put this in perspective, with only 1 user click, this semi-automated method can achieve a Dice of 0.64 for segmenting an unseen structure, colon cancer, in 126 Abdomen CT scans, outperforming the best automated model with a Dice of 0.56.

4.3.3. Summary

In this section, we covered the methodologies available for cost-effective image annotation. We first reviewed the active learning approach, which enables informed decisions as to which unlabeled images should be annotated first. While active learning methods are typically iterative and slow, recent works [Mahapatra et al. \(2018\)](#); [Zheng et al. \(2019\)](#) present a 1-shot, fast approach to active learning with comparable performance to the iterative counterparts, making active learning an even more attractive methodology. Nearly all active learning works reviewed in this survey base sample selection on informativeness and diversity of samples, neglecting the cost associated with annotating a sample. The exception is the work of [Kuo et al. \(2018\)](#) where the authors included annotation cost in their sample selection method. We believe that respecting annotation cost is fundamental to realistic active learning. We further reviewed interactive segmentation as a means of accelerating the annotation process. In particular, the work by [Sakinis et al. \(2019\)](#) was quite effective, where 1 user click led to a Dice of 0.64 for segmenting colon cancer, outperforming the best automated model with a Dice of 0.56. However, the efficacy of interactive segmentation methods in reducing annotation cost should be corroborated through more systematic user studies.

4.4. Leveraging Unlabeled Data

Unlabeled medical images, although lack annotations, can still be used in conjunction with labeled data to train higher-performing segmentation models. We have identified three scenarios wherein unlabeled medical images have aided medical image segmentation: 1) self-supervised pre-training where unlabeled images are used to pre-train a segmentation network; 2) semi-supervised learning with pseudo labels where unlabeled images are labeled by a segmentation model and then used as new examples during training; and 3) semi-supervised learning without pseudo labels where both labeled and unlabeled images are used jointly to train a segmentation model.

4.4.1. Self-supervised Pre-training

Self-supervised model pre-training has recently been studied as an alternative to transfer learning from natural images. The key idea consists of pre-training the model using unlabeled medical data, which is easier to obtain, and then fine-tune the pre-trained model for the target medical vision task using the limited labeled data available for training. Specifically, self-supervised pre-training consists of assigning surrogate or proxy labels to the unlabeled data and then training a randomly initialized network using the resulting

surrogate supervision signal. The advantage of model pre-training using unlabeled medical data is that the learned knowledge is related to the target medical task; and thus, can be more effective than transfer learning from a foreign domain (e.g., [Tajbakhsh et al. \(2019a\)](#) and [Ross et al. \(2018\)](#)).

Self-supervised learning methods differ in the composition of the surrogate task. Reviewing the literature, we have identified two types of surrogate tasks: 1) image-to-scalar where an encoder network is pre-trained for a surrogate image classification or regression task; 2) image-to-image where an encoder-decoder network is pre-trained for a surrogate image regression task such as image colorization or image denoising. While the former approach seems particularly suitable for a downstream image classification task, it can still be used to initialize the encoder of a segmentation network, in which case the decoder should be initialized with random weights. We have summarized the representative examples of both categories in Table 4, and further review them as follows.

Image-to-scalar: [Jamaludin et al. \(2017\)](#) propose longitudinal relationships between medical images as the surrogate task to pre-train model weights. To generate surrogate supervision, they assign a label of 1 if two longitudinal studies belong to the same patient and 0 otherwise. [Zhang et al. \(2017a\)](#) propose a surrogate task wherein two slices are randomly selected from a CT volume and then the encoder is to predict if one slice is above or below the reference slice. The pre-trained model is then fine-tuned for the task of body part recognition in CT and MR images. [Tajbakhsh et al. \(2019a\)](#) use prediction of image orientation as the surrogate task where the input image is rotated or flipped and the network is trained to predict such a transformation. The authors show that this surrogate task is highly effective for diabetic retinopathy classification in fundus images and lung lobe segmentation in chest CT scans. [Spitzer et al. \(2018\)](#) propose a new surrogate task that can be used to pre-train a Siamese network by predicting the 3D distance between two patches sampled from the same brain regions. The pre-trained model is then fine-tuned for cytoarchitectonic segmentation of the human brain. The authors use different sections of one MR scan for training and testing. The segmentation model trained from the self-supervised model achieves a Dice score of 0.8, outperforming the model trained from scratch with a Dice of 0.72. Similarly, [Gildenblat and Klaiman \(2019\)](#) suggest a surrogate scheme to pre-train a Siamese network by learning similarity between image patches. Specifically, the network is trained to distinguish between similar patches (nearby patches) and dissimilar patches (spatially distant patches). The pre-trained Siamese network is then fine-tuned for tumor tile retrieval in histopathology images.

Image-to-image: [Alex et al. \(2017\)](#) use noise removal in small image patches as the surrogate task, wherein the surrogate supervision was created by mapping the patches with user-injected noise to the original clean image patches. [Ross et al. \(2018\)](#) use image colorization as the surrogate task, wherein color colonoscopy images are converted to gray-scale and then recovered using a conditional GAN. The pre-trained

Table 4: Comparison between self-supervised training methods that can directly or indirectly aid medical image segmentation.

Publication	Network	Surrogate task		
		Type	Description	Annotation
Jamaludin et al. (2017)	Encoder	Image-to-scalar	Predict if two longitudinal studies belong to the same patient	1(same)/0(different)
Zhang et al. (2017a)	Encoder	Image-to-scalar	Predict the order of two slices random selected from the same CT scan	0(top)/1(bottom)
Tajbakhsh et al. (2019a)	Encoder	Image-to-scalar	Predict the degree of rotation applied to a chest CT scan	$\frac{\theta}{30^\circ}$ ($\theta \in \{0, 90, 180, 270\}$)
Spitzer et al. (2018)	Siamese	Image-to-scalar	Predict the distance between two patches sampled from the same MR image	Float distance
Gildenblat and Klaiman (2019)	Siamese	Image-to-scalar	Predict if two patches sampled from the same MR image are spatially near	1(near)/0(far)
Alex et al. (2017)	Encoder-decoder	Image-to-image	Learn how to remove noise from MR image patches	Original patch before injecting noise
Ross et al. (2018)	Encoder-decoder	Image-to-image	Learn how to colorize gray-scale colonoscopy frames	Original frame before removing color
Tajbakhsh et al. (2019a)	Encoder-decoder	Image-to-image	Learn how to colorize gray-scale tele-med skin images	Original image before removing color
Zhou et al. (2019b)	Encoder-decoder	Image-to-image	Learn how to restore the image from various degradation transformations	Original image before degradation
Bai et al. (2019)	Encoder-decoder	Image-to-image	Learn how to weakly localize anatomical landmarks in MR images	Approximate landmark positions

models are then fine-tuned for the task of instrument segmentation in colonoscopy videos with varying fractions of the training set. When only 25 images are used for fine-tuning, the instrument segmentation model pre-trained via self-supervised learning achieves a Dice score of 0.61, which outperforms the counterpart model pre-trained using Microsoft COCO dataset and the model trained from scratch, both with a Dice score of 0.57. However, weights pre-trained via self-supervised learning tend to lose their edge over randomly initialized weights when the size of the training set changes from 25 to 400 images. A similar study is also done by Tajbakhsh et al. (2019a) wherein colorization is used as a surrogate task for skin segmentation in tele-medicine images. While image colorization proved more effective than random initialization in training with both small (≈ 140 images) and large (≈ 1400 images) training sets, it was outperformed by transfer learning from ImageNet, presumably because the distance between tele-medicine skin images and ImageNet is small. Bai et al. (2019) propose anatomical position prediction as a self-supervised scheme. The landmarks are however obtained through an annotation-free process based on the relative views of image planes. The authors evaluate the effectiveness of the pre-trained models for the task of cardiac MR segmentation. In a low data regime where the training set has fewer than 50 MR images, self-supervised pre-training achieves a significant gain over random initialization. However, the performance gain becomes only marginal when the segmentation model is trained with 100 MR images.

The self-supervised learning methods described above are limited to a specific surrogate scheme. Models Genesis suggested by Zhou et al. (2019b) is a significant shift from this paradigm where a library of diverse self-supervised schemes, all formulated as an image restoration task, is used to generate self-supervision signal. The suggested framework is scalable to a large library of surrogate tasks, because all tasks in the library can share the same encoder and decoder during training, eliminating the need for task-specific decoders. The authors have evaluated Models Genesis for both image classification and segmentation in seven 2D and 3D medical datasets, demonstrating three and five points increase in IoU over 3D models trained from scratch for lung nodule segmentation and liver segmentation in CT scans, respectively. These results are significant because, unlike the previous works, the performance gains hold up when the models are trained using the full-size training datasets. One caveat,

Algorithm 3: Semi-supervised learning with pseudo annotations

Input : Small labeled dataset \mathcal{L} , unlabeled dataset \mathcal{U} , iteration times \mathcal{T} , masks generation function \mathcal{F}

Output: Updated model $\mathcal{M}_{\mathcal{T}}$

```

1  $\mathcal{M}_0 \leftarrow$  training base model with  $\mathcal{L}$ ;
2 for  $i \leftarrow 1$  to  $\mathcal{T}$  do
    /* generate pseudo segmentation masks */
3    $\mathcal{S}_i \leftarrow \mathcal{F}(\mathcal{M}_{i-1}, \mathcal{U})$ ;
4    $\mathcal{D}_i \leftarrow \mathcal{L} \cup \{(\mathbf{x}, s) | \mathbf{x} \in \mathcal{U}, s \in \mathcal{S}_i\}$ ;
5    $\mathcal{M}_i \leftarrow$  fine-tuning  $\mathcal{M}_{i-1}$  using  $\mathcal{D}_i$ ;
6 end
7 return  $\mathcal{M}_{\mathcal{T}}$ 

```

however, is that the models trained from scratch and those trained from pre-trained weights are all constructed without data augmentation. It is not clear how the performance gains change in the presence of data augmentation.

4.4.2. Semi-supervised learning with pseudo annotations

Semi-supervised learning with pseudo annotations consists of assigning pseudo annotations to unlabeled data and then training the segmentation model using both the labeled and pseudo labeled data. Pseudo labeling, serving as the backbone of this paradigm, is commonly done in an iterative manner wherein a model iteratively improves the quality of pseudo annotations by learning from its own predictions on unlabeled data. Semi-supervised learning with pseudo annotations has shown promising performance, producing models that outperform the counterparts trained using only labeled data.

Algorithm 3 shows the pseudo code for semi-supervised learning with pseudo annotations where one has access to a small labeled dataset and a fairly large unlabeled dataset. First, a base model is trained using limited labeled data. The base model is then applied to unlabeled data to generate pseudo segmentation masks. The limited labeled data is then merged with pseudo-labeled data to update the base model. This training paradigm alternates between the two steps above until a desired level of performance on the validation set is achieved. In a less common scenario, no initial labeled dataset is available for training, in which case, an unsupervised segmentation method such as K-means is used to generate pseudo

Table 5: Comparison between the methods based on semi-supervised learning with pseudo annotations for medical image segmentation. The suggested methods differ in how the initial labeled dataset is constructed, how pseudo annotations for unlabeled data are generated, and whether or not any special treatment is applied to the unreliable regions in pseudo annotation masks.

Publication	Initial annotations by	Pseudo masks generated by	Label noise handled by
Zhang et al. (2018b)	K-means	Single segmentation model	N/A
Bai et al. (2017)	Expert	Single segmentation model + CRF	N/A
Zhou et al. (2018a)	Expert	Ensemble segmentation model	N/A
Zhao et al. (2019b)	Expert	Single segmentation model	N/A
Nie et al. (2018)	Expert	Single segmentation model	Discriminator network
Min et al. (2018)	Expert	Ensemble segmentation model	Consensus by two parallel networks
Xia et al. (2020)	Expert	Ensemble segmentation model	Consensus by multi-view networks

masks for unlabeled data. While the semi-supervised learning methods based on pseudo annotations commonly follow the iterative process stated above, they differ in how they initialize the base model, how they generate pseudo masks, and whether or not they use a mechanism to handle label noise in pseudo segmentation masks. We have compared the semi-supervised learning methods that use pseudo annotations from these perspectives in Table 5, and further review them as follows.

Without initially labeled dataset: [Zhang et al. \(2018b\)](#) train a cyst segmentation model using unlabeled chest CT scans. Since the dataset is completely unlabeled, the authors generate the initial ground truth using K-means clustering followed by a refinement stage through graph cuts. The segmentation model is trained using the pseudo masks and then the model is applied back to the data to generate refined pseudo masks. The training process alternates between updating the segmentation model and refining pseudo masks. The authors train the segmentation model on 166 CT scans and use 17 CT scans including 5 mild, 6 moderate, and 6 severe cases for testing. In 3 iterations, the suggested method achieves 12-point increase in Dice over a model trained using the initial pseudo mask generated by K-means.

With initially labeled dataset: [Bai et al. \(2017\)](#) propose a two-step framework to segment the heart chambers in MR images. The training process alternates between two steps: 1) estimating the ground truth for unlabeled data using the current segmentation model followed by a refinement stage through the application of CRF, 2) updating the current model using both the labeled data with expert annotations and the unlabeled data with pseudo annotations. This approach is simple to implement; however, hindered by the quality of pseudo annotations, the resulting model achieves only a moderate level of improvement over the model trained using only labeled data. Similarly, [Zhou et al. \(2018a\)](#) propose an iterative framework, but, at each iteration, the authors train three segmentation models for the axial, sagittal, and coronal planes. Once trained, the three models scan each unlabeled 3D image slice-by-slice, generating three segmentation volumes, which are further combined through a majority voting scheme to form the final segmentation mask. The unlabeled images with their estimated segmentation masks are added to the labeled set to train three new segmentation models in the next

iteration. The authors test their semi-supervised paradigm in segmenting 16 structures in 80 contrast-enhanced abdominal clinical CT images in the portal venous phase. The training set consists of 50 labeled CT and 100 unlabeled CT scans. Under this data split, the suggested method achieves on average four points increase in Dice over the model trained using only the labeled data. The performance gain however drops to 1 point in Dice when the authors increase the size of labeled training set to 100 CT scans.

In the semi-supervised work by [Zhao et al. \(2019b\)](#) pseudo annotations are generated through data distillation where the segmentation masks obtained for different transformations of the same image are averaged to produce the final pseudo mask. The suggested model is trained for the task of brain region segmentation using 12 labeled and 749 unlabeled MR images. On a tests set with 20 MR scans, the suggested model achieves 1.6 points increase in Dice over the base model trained using only labeled data.

A limitation with the previous approaches is that the images that have expert annotation and images with pseudo segmentation masks are treated equally during training. As such, errors in the pseudo labels can degrade the quality of the resulting models. Recent methodologies overcome this limitation by estimating the reliability of pseudo annotations during training, by means of model consensus [Min et al. \(2018\)](#); [Xia et al. \(2020\)](#) or through the use of an evaluation network [Nie et al. \(2018\)](#). We cover these methods as follows:

[Min et al. \(2018\)](#) propose a two stream network where each stream has its own independent weights. During training, if a training sample receives the same class prediction from both streams, then the sample is deemed as easy or hard, in which case it will not contribute to the overall loss, where the training samples refer to each individual pixel. The rationale is that the easy examples do not add much value to the model and the hard examples may have label noise; therefore, it is safe to exclude them from backpropagation. To obtain the pseudo segmentation masks, the authors propose a hybrid method based on model distillation [Gupta et al. \(2016\)](#) and data distillation [Radosavovic et al. \(2018\)](#), which essentially consists of model-ensembling and test-time data augmentation. The authors use two public datasets for evaluation: BraTS 2015 [Menze et al. \(2014\)](#) with 244 MR images for training and 30 images for testing, and HVSMT 2016 with 10 MR images

for training and 10 images for testing. The results show that the suggested semi-supervised learning framework based on pseudo-labeling and the two-stream network is noise-resilient, significantly outperforming fully supervised models under varying levels of label noise present in labeled images.

Nie et al. (2018) use only the reliable regions of the pseudo segmentation masks during training. Specifically, they propose a framework consisting of a segmentation network (generator) and a confidence network (discriminator), which are trained through an adversarial game. The discriminator, a fully convolutional network, serves two purposes: 1) distinguishing between ground truth and predicted masks at the pixel level, 2) providing a confidence (reliability) value for each pixel in the predicted mask. The former functionality is used during adversarial training whereas the latter functionality is used to identify reliable regions in the pseudo masks of unlabeled data. During training, the pseudo mask for an unlabeled image is first masked by the binarized confidence map and is then used as ground truth to compute the segmentation loss. The authors show the effectiveness of the suggested framework over a pure supervised approach across multiple datasets.

Xia et al. (2020) have suggested a semi-supervised framework based on co-training of multiple networks wherein pseudo annotations are generated as the consensus of network predictions in the ensemble. Specifically, N views of the same input are fed to N parallel convolutional networks, which each is trained using labeled data and the corresponding ground truth, as well as, unlabeled data with the pseudo annotations generated through the combination of the predictions from the other $N - 1$ networks. To mitigate the unreliable regions in pseudo annotations, network predictions are combined through an uncertainty-aware scheme where each prediction is weighted by its uncertainty. The authors use the dropout scheme to estimate uncertainty for predictions—a common scheme in active learning, see Section 4.3.1. For pancreas segmentation in the NIH dataset (62 training and 20 test CT scans), the authors report seven points and five points increase in Dice over a full supervised model, when 10% and 20% of the training set is used as the initial labeled training set.

4.4.3. Semi-supervised learning without pseudo annotations

Semi-supervised learning without pseudo annotations consists of training a model with both labeled and unlabeled data, where the unlabeled data generate a supervision signal through an unsupervised loss function. In this paradigm, the domain of unlabeled data may be from a different domain or from the same domain as the labeled dataset. The former is commonly known as unsupervised domain adaptation, which aims to mitigate the domain shift problem by adapting the model to a target domain. We discuss unsupervised domain adaptation methods in Section 4.2.2. The latter enables training the model in the source domain using both labeled and unlabeled data, increasing the effective size of the training set, mitigating the problem of limited annotations in the source domain. In this section, we focus on this form of semi-supervised learning.

Algorithm 4 shows the pseudocode for semi-supervised learning without pseudo annotations in its most general form.

Algorithm 4: Semi-supervised learning without pseudo annotations

Input : Limited labeled dataset \mathcal{L} , unlabeled dataset \mathcal{U} , shared backbone \mathcal{M}_c , branch model and loss function for labeled data \mathcal{M}_l, ℓ_l , branch model and loss function for unlabeled data \mathcal{M}_u, ℓ_u

Output: Fine-tuned model \mathcal{M}

- 1 $\zeta_l \leftarrow \ell_l(\mathcal{M}_l(\mathcal{M}_c(\mathcal{L})))$;
 - 2 $\zeta_u \leftarrow \ell_u(\mathcal{M}_u(\mathcal{M}_c(\mathcal{U})) + \ell_u(\mathcal{M}_u(\mathcal{M}_c(\mathcal{L})))$;
 - 3 minimize($\zeta_l + \zeta_u$);
 - 4 **return** \mathcal{M}
-

As seen, the semi-supervised framework consists of two loss functions: a supervised loss function to which only labeled data contribute; and an unsupervised loss function or a regularization term, which is computed for both labeled and unlabeled data. The total loss is the summation of the two terms, which is minimized for batches of labeled and unlabeled data.

We have listed the representative semi-supervised methods for medical image segmentation in Table 6. As seen, the suggested methods differ in terms of the unsupervised task, which can be as simple as image reconstruction or transformation consistency or representation similarity based on adversarial loss. For better readability, we have grouped the related semi-supervised methods by the underlying unsupervised task and explain them as follows:

Via image reconstruction: Chartsias et al. (2018) propose a solution to the problem of domain shift based on a disentangled image representation where the idea is to separate information related to segmenting the structure of interest from the other image features that readily change from one domain to another. By doing so, the segmentation network focuses on the intrinsic features of the target structure rather than variations related to imaging scanners or artifacts. The authors show that the suggested framework is highly effective for myocardial segmentation in low-data regime, but the performance gap closes as the size of training set increases.

Chen et al. (2019c) suggest a semi-supervised learning framework with one encoder and two decoders. The first decoder is used for the segmentation task and is trained with the labeled data. The second decoder is trained using unlabeled data for the task of class-specific image reconstruction. Specifically, given a k -class segmentation problem, the reconstruction decoder generates k maps, which each is compared against the input image multiplied by the corresponding segmentation mask obtained from the segmentation decoder. For tumor segmentation in the BraTS dataset Menze et al. (2014) (120 training and 50 test MR scans), the authors report six and seven points increase in Dice over supervised model when 20 and 50 labeled MR images are used for training. The semi-supervised model, however, continues to outperform the supervised model by four points in Dice even when the entire large set of the labeled dataset is used for training—a significant finding rarely reported before.

Table 6: Semi-supervised methods suggested for medical image segmentation that do not use pseudo annotations. The suggested methods combine the segmentation task with an unsupervised task, allowing the model to use both labeled and unlabeled images during training.

Publication	Unsupervised task	Description
Li et al. (2019b)	Transformation consistency	Segmentation model is trained to achieve equivariance to image rotation or flipping
Bortsova et al. (2019)	Transformation consistency	Segmentation model is trained to achieve equivariance to elastic image deformation
Yu et al. (2019)	Transformation consistency	Segmentation model is mentored by a mean teacher network to achieve equivariance to image perturbations
Cui et al. (2019)	Transformation consistency	Segmentation model is mentored by a mean teacher network to achieve equivariance to image perturbations
Chen et al. (2019c)	Image reconstruction	Segmentation model is trained along with a class-specific image reconstruction network
Chartsias et al. (2018)	Image reconstruction	Segmentation model decomposes an image into a mask and a vector and then feeds them to image reconstruction
Sedai et al. (2017)	Representation similarity	Segmentation model is trained to mimic the latent space of an autoencoder that is trained by unlabeled data
Zhang et al. (2017b)	Representation similarity	Segmentation model is trained adversarially to similarize the segmentation of labeled and unlabeled images
Baur et al. (2017)	Representation similarity	Segmentation model is trained to bring the feature embedding of labeled and unlabeled images close
Mondal et al. (2018)	Representation similarity	Segmentation model is trained to maximize the similarity between the logits of labeled and unlabeled data

Via transformation consistency: It is known that convolutional networks are inherently not rotation equivariant¹. The recent semi-supervised learning frameworks have turned this weakness of regular convolutional networks into an opportunity to leverage unlabeled data. Specifically, they attempt to achieve transformation equivariance by minimizing a transformation consistency loss, to which both labeled and unlabeled data can contribute. Let x , T , S denote the input image, an image transformation, and the segmentation network, respectively. The transformation-consistent regularization is formulated as $\|S(T(x)) - T(S(x))\|$, which is essentially the mean squared error loss between the segmentation map of the transformed image, $S(T(x))$, and the transformed segmentation map of the original image, $T(S(x))$. By imposing this additional regularization term, not only does the model behave more predictably, but also it can utilize the unlabeled data available for training. In what follows, we review how transformation consistency has been used in modern semi-supervised learning methods.

Li et al. (2019b) propose a semi-supervised learning framework consisting of a segmentation loss whose optimization requires labeled data, and a rotation equivariant loss where both labeled and unlabeled data can contribute to. Simply, if an image, being labeled or unlabeled, is rotated by 90 degrees, then the resulting segmentation map should also appear with 90 degrees of rotations with respect to the segmentation mask of the original image. Transformation equivariance is also adopted by Bortsova et al. (2019) where the segmentation model is trained to achieve equivariance to elastic deformation. Performance evaluation on multiple datasets show that both methods above are effective in boosting segmentation performance in low data regime; however, the performance gains tend to be limited in the presence of large labeled training sets.

The works above enforce consistency by imposing constraints on the outputs of the segmentation network for the original and the transformed images. A different approach to ensure transformation consistency is through the mean teacher paradigm. The student network is the segmentation model, which receives the original image. The teacher network has the same architecture as the student network and receives a

transformed version of the image sent to the teacher network. The unsupervised loss minimizes the dissimilarity between the segmentation masks of the original and transformed images, which are generated by the teacher and student networks, respectively. In this paradigm, the student network is trained as usual by minimizing the segmentation and consistency loss; however, the teacher network is not trained through back-propagation—it merely tracks the weights of the student network through an exponential moving average rule. Mean teacher paradigm, a.k.a self-ensembling, is expected to outperform the previous paradigm where the segmentation network serves as both teacher and student. This is because the teacher network typically outperforms the student network; and thus, it can generate more reliable targets for the consistency loss. In the following, we review the self-ensembling methods suggested for medical image segmentation.

Cui et al. (2019) adopts the mean teacher paradigm for the task of stroke lesion segmentation in MR images. In this method, the segmentation consistency is measured under additive and multiplicative Gaussian noise. For training, the authors use a dataset with 20 labeled and 196 unlabeled training subjects. Test results on MR images from 30 subjects demonstrate that the semi-supervised model achieves three points increase in Dice over a supervised model, further outperforming semi-supervised methods by Zhang et al. (2017b). This mean teacher model is further extended by Yu et al. (2019) where the consistency loss is masked through an uncertainty map. The idea is that regions with low uncertainty should contribute to the segmentation consistency loss. The authors estimate segmentation uncertainty by using Monte Carlo dropout Kendall and Gal (2017) in the teacher network. For the task of atrial segmentation in a dataset with 80 training and 20 test MR images, the authors report four points increase in Dice over a supervised model trained using 16 labeled images. This improvement is however similar to that of other competing semi-supervised methods used for comparison (e.g., Li et al. (2019b)).

Via representation similarity: Semi-supervised learning method often use adversarial loss functions to bridge the dissimilarities between the representations of labeled and unlabeled images, thereby leveraging unlabeled data during the course of training. In this paradigm, the term representation may refer to the feature maps at the latent space of an encoder Baur et al. (2017); Sedai et al. (2017), or to the

¹Researchers have attempted to instill this property through various approaches such as group equivariant convolutional neural networks Cohen and Welling (2016), which has also proved effective in segmenting histopathology images Veeling et al. (2018).

final segmentation map of a decoder [Zhang et al. \(2017b\)](#); [Mondal et al. \(2018\)](#). We present a detailed description of these methodologies as follows.

The semi-supervised framework suggested by [Baur et al. \(2017\)](#) consist of a U-Net with two loss functions: a Dice-based segmentation loss that is computed based on the labeled data; and an embedding loss, which, given a batch of labeled and unlabeled data, brings the feature embedding of the same-class pixels as close as possible while pushing apart the feature embedding of the pixels from different classes. To identify same-class pixels between labeled and unlabeled images, the authors assume the availability of a noisy label prior for unlabeled images. Also, to reduce the number of pair-wise comparisons between feature embedding of all pixels within the batch, they employ a pixel sampling scheme. The suggested semi-supervised framework proves promising in improving the segmentation of multiple sclerosis in the presence of limited data and domain shift. However, one caveat is that the suggested method is evaluated only in a low data regime where the labeled and unlabeled training sets have images from 3 and 9 subjects, respectively.

[Sedai et al. \(2017\)](#) propose a semi-supervised learning framework consisting of a segmentation network and an auto-encoder. The training process begins with training a variational auto-encoder, which stores the knowledge learned from the unlabeled images in its latent space. Next, the segmentation network, which is also a variational auto-encoder, is trained using the labeled data. To leverage the knowledge learned from the unlabeled data, in addition to the segmentation loss, the segmentation network benefits from an l2-loss between its latent feature vector and the one generated by the reconstruction network for a given labeled image. The authors evaluate this framework in segmenting optic cup segmentation in fundus images using an unlabeled training set of 11400 images and a labeled training set of 400 images. On a test set with 200 images, the semi-supervised model achieves four points and one point increase in Dice over the supervised model, when 12.5% and 100% of the labeled set is used for training, respectively.

[Zhang et al. \(2017b\)](#) propose a semi-supervised learning framework according to an adversarial game between a segmentation network (U-Net) and an evaluation network (encoder). Given an input image, the segmentation network generates a segmentation map, which is then stacked with the original image and fed to the evaluation network, resulting in a quality score. During training, the segmentation network is updated with two objectives: 1) minimizing the segmentation loss for the labeled images and 2) making the evaluation network assign a high quality score to the unlabeled images. On the other hand, the evaluation network is updated so as to assign a low quality score to unlabeled images but a high quality score to labeled images. Owing to this adversarial learning, the segmentation network enjoys a supervision signal from both labeled and unlabeled images. The authors evaluate this semi-supervised learning framework in two applications, one of which being gland segmentation in histopathology images, where the labeled and unlabeled training sets consist

of 85 and 100 images. The suggested model however yields mixed results, yielding comparable Dice to a supervised model on the larger test set (60 images) while achieving 1 point increase in Dice on the smaller test set (20 images).

[Mondal et al. \(2018\)](#) propose a semi-supervised framework that integrates labeled and unlabeled images for the task of brain tissue segmentation in MR images. For this purpose, the authors train the segmentation network by introducing an additional fake class, resulting in a $k + 1$ class segmentation problem where k is the number of classes present in the dataset. During training, the segmentation network seeks to maximize the probability of the correct class for each pixel in the labeled images. For unlabeled images, the segmentation network minimizes the probability of each pixel belonging to the fake class, which has the effect of maximizing the probability by which an unlabeled pixel belongs to one of the k classes. The suggested method proves effective in segmenting brain tissues from MR images when the training set contains only a few annotated images.

4.4.4. Summary

In this section, we reviewed three strategies that enable training a segmentation model with both labeled and unlabeled data. We started with self-supervised learning, which consists of pre-training the segmentation network using unlabeled medical images followed by fine-tuning the pre-trained model using the target labeled dataset. Self-supervised learning offers several advantages: 1) demonstrated performance gains over the counterpart models trained from scratch; 2) ease of implementation owing to the intuitive underlying proxy tasks; and 3) ease of use, because no or only minor architectural changes to the segmentation network is required.

We further reviewed semi-supervised learning with pseudo annotations where the model learns from its own prediction on unlabeled images. The suggested methods often show only moderate performance gains over the counterparts trained using only labeled images. This is because model-generated annotations can be noisy, which has detrimental effects to the subsequent segmentation model. This limitations has been recently addressed in [Min et al. \(2018\)](#); [Nie et al. \(2018\)](#), but at the expense of relatively complex segmentation architectures.

Semi-supervised learning without pseudo annotations was the third strategy we reviewed, which uses unlabeled data along with the labeled data during training. Since these methods accommodate the segmentation task for the labeled data and an unsupervised task for the unlabeled data, they typically consist of complex neural architectures. Nevertheless, these semi-supervised schemes are effective in coping with limited labeled training sets, improving the Dice score by a couple of points in most cases. One caveat, however, is that these methods are not as effective when the training set grows in size, suggesting that one should not be overoptimistic about the capabilities of these methods. Compared to the previous strategy, these methods do not attempt to generate annotations for the unlabeled images; as such, they are not vulnerable to annotation noise.

4.5. Regularized Training

Having a large number of parameters, deep supervised models are prone to over-fitting, particularly in the absence of large training sets. The traditional regularization to the problem of over-fitting is weight regularization whereby the network is encouraged to keep the weights small, resulting in a simpler and more robust model. While effective, weight regularization is only one form of model regularization. In this section, we cover other forms of regularization: altered image representation, multi-task learning, and shape regularization.

4.5.1. Altered Image Representation

Altered image representations consist of projecting or transforming the images into a more informative or compact representation, which present deep models with an easier problem to solve, thereby reducing the need for large training sets. Informative representations can be particularly effective for 2D medical image segmentation whereas compact representations can benefit 3D applications where the curse of dimensionality requires large annotated datasets. This section reviews altered representations for both 2D and 3D images.

Altered 3D image representation: Training segmentation models with altered 3D image representations include training 2D models with multi-scale and multi-view patches Wang et al. (2017), fusing 2D models trained for the three clinical views Xia et al. (2018), training a 2D model with a 2.5D image representation Angermann et al. (2019), and finally training a 3D model with a 3D representation augmented with handcrafted features Ghafoorian et al. (2017). We explain these methods in more detail as follows.

Wang et al. (2017) make use of multi scale 2D patch-based pixel predictions for the task of lung nodule segmentation. The network has three shallow branches, one for each of the three orthogonal clinical views that share the same central pixel. Each branch is fed a 2D 2-channel input that captures the nodule at two different scales. The three branches are then fused to provide a binary prediction for the central pixel of the patch. Thus, there are six new 2D patches used for every voxel in the 3D volume being segmented. The segmentation results for all voxels are finally put together to obtain the 3D segmentation mask. Testing on 393 nodules from the LIDC dataset, they achieve 7% increase in Dice over GrabCut; however, they have not compared their method against a single view CNN approach.

Xia et al. (2018) propose a 2-stage approach where the first stage uses a set of 2D segmentation networks whose outputs are further fused in the second stage through a 3D volumetric fusion network. The 2D networks generate slice-by-slice predictions along each of the 3 orthogonal views—axial, sagittal and coronal. The stacks of predicted segmentation masks for the 3 views are then concatenated with the original image, creating a 4-channel input to the second network, which learns to fuse the predictions to produce the final 3D prediction. For the task of pancreas segmentation, the authors experiment with 4-fold cross validation on the NIH pancreas segmentation dataset, which contains 82 abdominal CT

volumes. For their experiments on multi-organ segmentation, they curated an in-house dataset of high resolution abdominal CT scans and tested their approach on 50 scans. In both scenarios, the suggested method improves Dice score by 1% over baselines that use majority voting for volume fusion.

Angermann et al. (2019) make use of intensity projections, specifically maximum intensity projections (MIP) at multiple angles, which are then fused to create a 2.5D representation of magnetic resonance angiography images. The authors use their approach for the task of volumetric blood vessel segmentation with 18 test volumes. However, the authors have not demonstrated a significant gain over the 2D and 3D performance baselines.

Ghafoorian et al. (2017) use an image representation based on registered T1 and FLAIR MR images augmented with dense handcrafted features to segment white matter hyperintensities. On a test set of 46 cases, their multi-scale architecture equipped with the hand-crafted features achieves 6% increase in Dice over their single scale baseline that does not incorporate the handcrafted features. Noteworthy, the improved segmentation performance is mainly due to the contribution of handcrafted features rather than the multi-scale paradigm.

Altered 2D image representation: The aforementioned methods offered altered representations for 3D images; however, even problems that are inherently 2-dimensional can benefit from using a different representation. Fu et al. (2018b) utilize an image representation based on the polar coordinate system for the purpose of joint cup and disc segmentation in fundus images. Specifically, the authors use a circular image crop around the cup and disc region, which is then converted to a rectangular image through a transformation from Cartesian to polar coordinates. Scale-based data augmentation is performed by varying the radius of the circle prior to coordinate conversion. The authors have used the area under the ROC curve for evaluating the binary glaucoma classification performance using the cup to disc ratio. They test their model on 325 images from the ORIGA dataset and the entire SCES dataset containing 1676 fundus images. The suggested image representation enables a 4% gain in AUC compared with the existing state of the art trained using the standard Cartesian plane image representation.

4.5.2. Multi-task Learning

Multi-task learning Zhang and Yang (2017) refers to the paradigm in which multiple tasks are derived from a single learned representation. In modern applications, this can be realized by a single feature extractor (encoder) on which multiple tasks (e.g. classification, detection, segmentation) are performed. Intuitively, this paradigm encourages the encoder network to learn a latent representation that generalizes across the required tasks, with each task serving as a regularizer for the others. The studies outlined below demonstrate that adding a parallel task generally results in improved segmentation performance at little or no cost in terms of additional data. These tasks may be supervised (e.g. classification, detection),

requiring additional annotations), or unsupervised (e.g. image reconstruction) with no additional labeling required.

Most multi-task learning applications to medical image segmentation involve a variant of the U-net. The upsampling (segmentation) branch can be understood as just one of multiple output “heads” connected to a feature extractor, which allows for a natural extension to other tasks from the abstract feature space. [Mehta et al. \(2018\)](#) apply such a multi-task U-net to segment different tissue types in breast biopsy histopathology images, where an additional classification head is trained to classify whether the image is malignant or not. Simply adding this additional branch, which encouraged the model to learn a feature space relevant to diagnosis in addition to tissue segmentation, significantly improves the IoU of the vanilla network by 7%.

Similarly, [Jaeger et al. \(2018\)](#); [Huang et al. \(2018b\)](#) propose a joint segmentation and detection framework. [Huang et al. \(2018b\)](#) use their method for colorectal tumor segmentation in MRI volumes. Their proposed model resembles Mask-RCNN [He et al. \(2017\)](#), in which a global image encoder network detects regions of interest (ROIs), and a local decoder performs tumor segmentation on the proposed regions. The feature pyramid representing each ROI is passed to the local decoder, which, unlike Mask-RCNN, only segments the region of interest. The authors show that the local (rather than global) decoding approach preserves spatial details as well as decreases GPU footprint. This approach outperforms other U-net variants by several points and the popular Mask R-CNN algorithm by 20 points when the Dice score is used for performance evaluation.

[Sun et al. \(2018b\)](#) apply multi-task learning to brain tissue segmentation, combining the segmentation task with image denoising. The base architecture of their model can still be described as a modified U-net, in which a shared encoder generates a latent feature representation for two separate decoders (for image reconstruction and segmentation). However, instead of training the network from scratch, Sun and colleagues pre-train the reconstruction head before training the full model end-to-end. By jointly performing image reconstruction with segmentation, they observed improved segmentation performance in all types of brain tissue across different metrics.

The objective function in the multi-task paradigm is generally presented as the summation of the loss functions for each respective task, implicitly giving each an equal weight. In a recent work, [Li et al. \(2019a\)](#) present a network for echocardiographic sequence segmentation comprised of a feature pyramid based CNN for segmentation and classification. They introduce an aggregation loss which frames the final loss as a weighted combination of the segmentation and classification loss functions, allowing these weights to be empirically calculated during training. Their ablation studies show that multi task learning (segmentation and image-level classification) significantly increase segmentation when compared to the same network without the additional classification task.

One drawback of the above approaches is that the companion task (classification or detection) requires additional

labels for each image. Image reconstruction can be considered an unsupervised task that still provides the regularization benefits of multi-task learning. [Myronenko \(2018\)](#) propose a framework combining image reconstruction and segmentation for the task of brain lesion segmentation. The proposed model is a variational auto-encoder with an asymmetrically large encoder backbone and two decoders: the first decoder is trained to reconstruct the input MR image whereas the second decoder generates the segmentation maps. The suggested method outperforms other modifications such as CRF post-processing as well as sophisticated test-time data augmentation, winning the first place in the 2018 BraTS challenge [Menze et al. \(2014\)](#).

In addition to providing robustness to the learned feature representation via regularization, the multi-task paradigm provides a feasible framework for consolidated biomedical image segmentation. As Harouni and colleagues [Harouni et al. \(2018b\)](#) note, given the sheer number of potential conditions, a single model per condition is not a scalable approach for clinical use. As a proof of concept, Harouni and colleagues use an architecture similar to Y-net [Mehta et al. \(2018\)](#) to segment different organs in several different imaging modalities using a single network. A single U-net is trained to segment nine different targets encountered in thoracic imaging, which is complemented by a classification branch trained to determine the input domain (e.g., CT, MRI, Ultrasound). While this model does not exceed the state of the art performance for any one given modality or target, performance is competitive across all domains. The authors also report that the presence of the image classification branch results in slightly improved segmentation performance.

4.5.3. Shape Regularization

Shape defines a region of interest (ROI) in segmentation problems under certain constraints, e.g. smooth and semantically sound. Such constraints can be effectively encoded as regularization towards more realistic appearance of the segmentation output, especially when well-annotated data is scarce. Specifically, shape regularization consists of imposing a prior, highlighting certain geometric and structural characteristics, on the segmented ROIs, by operating either at pixel-level with an emphasis on shape and boundary explicitly, or in depth to capture high level features related to semantic meanings. In this section, we refer to the methods serving the former and latter objective as *Shallow regularization* and *Deep regularization*, respectively.

Shallow shape regularization: Shallow shape prior may regularize boundary pixels towards a certain class of shapes. [Mirikharaji and Hamarneh \(2018\)](#) leverage a star shape prior via an extra loss term on top of a binary cross entropy loss. To regularize a segmented ROI towards a star shape, any point on the linear path in between the ROI center and an interior point is expected to be interior as well (Fig 3 a & b), ensuring a smooth segmentation mask without holes. This definition comprises a broad class of objects even including convex shapes as a special case. With this additional term, authors evaluate the effectiveness of the star prior for skin lesion segmentation on

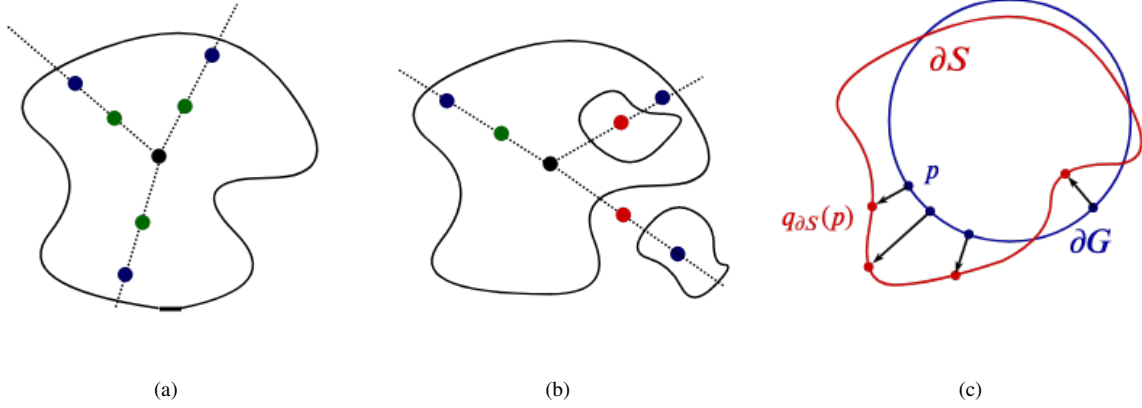


Figure 3: Shape regularization can combat the limited annotation problem by imposing additional constraints on predicted segmentation masks. Two common shape regularization methods are 1) star shape prior where any point in between the center and an interior point is constrained to be interior, and 2) boundary regularization. (a) An example of a segmented region that meets star shape prior. The black circle indicates the center of the segmented shape, the blue circles refer to interior points near the boundary, and the green circles are interior points that satisfy the star shape criteria. (b) An example of a segmented region with a hole and an isolated island, which does not meet requirements of star shape prior. The red circles indicate the pixels that lie exterior to the segmented region. (c) Boundary regularization improves segmentation accuracy around boundaries by minimizing point-wise deviation between the segmentation mask S relative to the ground truth G .

the ISIC 2017 dataset (2000 training 600 test images) and report a 3.0% gain in Dice using U-net as segmentation network over the same network without star shape regularized loss.

Another class of shallow priors operate on boundary pixels to further improve segmentation accuracy around the boundaries. Boundary points, the first order derivative of a region, better capture the proximity of two shapes by inducing an extra penalty term between the estimated and expected pixels along the boundary. Inspired by the optimization technique for computing gradient flows of curve evolution, [Kervadec et al. \(2019\)](#) introduce a non-symmetric L_2 loss to regularize boundary deviation of the segmentation mask S relative to the ground truth G ,

$$\text{Dist}(\partial G, \partial S) = \int_{\partial G} \|q_{\partial S}(p) - p\|^2 dp, \quad (1)$$

where a boundary point p on ∂G (boundary of GT) is aligned against its counterpart q on ∂S (boundary of prediction), which is written as $q_{\partial S}(p)$, such that $p \rightarrow q$ is norm to GT boundary at point p (see Fig 3 c). By using the boundary loss for brain lesion segmentation, authors evaluate on two MRI datasets (ISLES with 74 training plus 20 testing and WMH of 50 training plus 10 testing) and report an 8% gain in Dice and a 10% gain in Hausdorff score over a baseline that uses generalized Dice as the loss function on ISLES dataset compared to marginal improvement on the WMH dataset.

[Karimi and Salcudean \(2019\)](#) explore three approximations to Hausdorff distance such that it can be directly minimized. The authors report performance on multiple applications including 2D prostate ultrasound (450/225), 3D prostate MRI (80/30), 3D Liver CT (100/31) and 3D Pancreas CT (200/82), resulting in 18% to 45% reduction in Hausdorff distance without degrading other performance metrics such as Dice similarity coefficient.

More recently, [Duan et al. \(2019\)](#) propose a refinement

approach following a segmentation network that utilizes shape information by registering a cohort of atlas masks to the target segmentation mask. In their work, the first step consists of a 2.5D FCN trained to segment ROIs and localize 6 landmark points, e.g. center of the mitral valve. This step is conducted on both high-resolution (HR) and low-resolution (LR) cardiac MR images whereas HR volumes will later on be used as atlases. In the refinement stage, a sequence of landmark alignment, atlas selection and deformable registration are used to map a cohort of HR volumes to the target LR volumes, then labels from this cohort of atlases are fused to derive a shape-refined mask of LR images in the HR mode. The authors evaluate on MR scans of both healthy and pathological cases. For healthy cases which only contain HR images, LR images are simulated by downsampling and adding artefacts and ground truth masks in HR are used for evaluation. With a 1000/600/231 data split, the 2.5D FCN trained on the LR cases with refinement achieves comparable performance relative to the 2.5D FCN trained on the HR cases, trailing by 2.0% for most regions in Dice and 0.5mm worse in Hausdorff distance. As for pathological cases, 629 volumes are in the LR mode only and another 20 volumes have both HR and LR images. For the task of myocardium segmentation, the authors report performance superior to 3D-ACNN [Oktay et al. \(2017\)](#), achieving 4.3% increase in Dice and 4.15mm (40% less) improvement in Hausdorff distance. However, the refinement stage is computationally expensive, taking 15-20 minutes per case with their multiple CPU implementation.

Shape priors are also leveraged in training with partially labeled data. [Zhou et al. \(2019a\)](#) tackle the problem of multi-organ segmentation when more datasets are available as single organ annotated. Specifically, the proposed method assumes that the average organ size distribution approximates what is learned from fully labeled data, therefore, it can be utilized as a organ-specific prior guiding the training on single

organ datasets. In their experiments, an FCN is initialized on 30 fully labeled abdominal CT scans to segment 13 anatomical structures, followed by partially labeled datasets on spleen, pancreas and liver, each of which containing 40 scans. Their approach outperforms a naive partial supervision implementation, which does not benefit from shape prior regularization, by 1.69% in Dice with ResNet-101 as backbone for 2D task and by 0.45% in Dice using 3D U-Net as the backbone models, both based on 5-fold cross-validation.

Deep shape regularization: Shape regularization can also be applied to high level semantic features. Compared to shallow approaches, deep regularization, a.k.a deep supervision or deep priors, is less prone to image noise and more semantically and structurally aware. Ravishankar et al. (2017) incorporate deep prior within segmentation framework where a segmentation FCN is followed by a shape regularization FCN, which functions as a *convolutional denoising autoencoder* (CDAE), consisting of an encoder that projects the segmentation mask to the shape space and a decoder that samples a segmentation mask from the shape space. In addition to the reconstruction loss, the regularization FCN has a projection loss that constraints ground truth and predicted segmentation to have similar encodings in the shape space. Combining both data augmentation and deep regularization, Ravishankar et al. (2017) report a 4.66% gain in Dice relative to a vanilla U-Net segmenting kidney on 2D ultrasound B-mode images (100 training and 131 testing).

Oktay et al. (2017) adopts a similar cascaded architecture with a major difference: the regularization FCN is first pre-trained as an auto-encoder with ground truth masks, and then only its frozen encoder is used as a regularizer during training the segmentation network. Therefore, the objective function reduces to a regular segmentation loss and a shape projection loss. The suggested model achieves 1.2% and 2.0% improvement respectively in Dice over Ravishankar et al. (2017) for 3D endocardium and myocardium segmentation on a cine-MR dataset (1000 training and 200 testing). The authors attribute the inferior performance by Ravishankar et al. (2017) to over-regularization, which they have overcome by replacing CDAE with a frozen encoder during training.

Dalca et al. (2018) suggest a segmentation VAE that leverages shape prior in order to learn from unpaired images and segmentation masks. The VAE consists of an image encoder, which is initialized from scratch, and a frozen decoder, which is selected from an auto-encoder that has previously been trained for the task of mask reconstruction on 5000 T1-weighted brain MRI scans. Since the VAE uses a segmentation decoder, it generates a segmentation mask given an input MR image. However, the input MR images have no corresponding ground truth segmentation; therefore, the VAE is trained by minimizing the L2-loss between the input MR image and the predicted segmentation after being transformed through a 1x1 convolution block. During inference, the authors use the decoder output as the segmentation result. For the task of brain structure segmentation, the suggested method is evaluated on 9000 MRI scans, achieving Dice scores

ranging between 0.50 and 0.80 without any comparison against supervised methods.

He et al. (2019) propose a segmentation network that benefits from priori anatomical features. To capture anatomy priors, the authors first train a denoising autoencoder with unlabeled data. To embed the shape prior in the segmentation network, the authors concatenate the latent space of the segmentation network with priori anatomical features generated by the frozen encoder of the autoencoder. The authors use 26 labeled and 118 unlabeled abdominal CTA volumes for training and report 1.0% gain in Dice over the same architecture without anatomy priori on a test set of 26 volumes.

4.5.4. Summary

In this section, we covered three forms of regularization. We first reviewed altered image representations, where regularization is applied to the input space. This form of data regularization results in a lower dimensional input space or an altered input space that facilitates the task of representation learning for the model particularly in the absence of large labeled datasets. We then reviewed multi-task learning for medical image segmentation, which leads to consistent improvement over the single-task segmentation models and further enables a consolidated framework for multi-modality multi-condition medical image segmentation. Lastly, we reviewed shape regularization, which imposes a shallow or deep shape prior on the predicted segmentation results. While no prior works have considered the combination of the above three forms of regularization, these approaches are independent and can potentially offer complementary advantages. Also, except for multi-task learning which requires additional annotations, input space regularization and shape regularization require no further annotations; and thus, can be taken advantage of at the cost of changing the data pipeline and minor architectural changes, respectively.

4.6. Post segmentation refinement

Variants of auto-encoders have recently been adopted for automatic error correction in medical images Larrazabal et al. (2019); Tajbakhsh et al. (2019b), outperforming conditional random fields (CRFs) especially in the presence of domain shift and limited annotations. Nevertheless, CRFs are still the most commonly adopted and recognized approach to refine segmentation masks of both natural images (Schwing and Urtasun (2015), Chen et al. (2017) and Zheng et al. (2015)) and medical images (Roth et al. (2015), Chen and de Bruijne (2018) and Wachinger et al. (2018)). In the following, we briefly explain CRFs and then cover the papers that have used variants of CRF for medical image segmentation.

To obtain more realistic predicted masks, a CRF model incorporates two regularization terms: a smoothness term that removes small isolated regions, and an appearance term that ensures nearby pixels with similar color will more likely belong to the same class. The segmentation result, inferred as a maximum a posteriori (MAP) estimate from the CRF defined across all pixels, is expected to capture both local features and

spatial dependency more holistically. As a consequence, CRF is able to refine a collection of inaccurate and coarse pixel-level predictions, producing sharp boundaries and fine-grained segmentation masks.

Concretely, a CRF models pixel-wise labels, X , collectively as a random field that is conditioned upon image/volume intensities, I . This CRF can be characterized by its potentials, consisting of unary and pairwise terms [Krähenbühl and Koltun \(2011\)](#),

$$E(\mathbf{x} | \mathbf{I}) = \sum_i \phi_u(x_i) + \sum_{i \neq j} \phi_p(x_i, x_j). \quad (2)$$

The unary potential $\phi_u(x_i)$ is computed independently per pixel, which incorporates shape, texture, location and color descriptors. The existing variants of CRF differ in terms of the definition of the pairwise potential term, $\phi_p(x_i, x_j)$, and the underlying optimization technique. These variants include *Local CRF*, which considers neighboring pixels only, i.e. $j \in \text{neighbor}(i)$; *Fully Connected CRF* (FC-CRF), which considers all pixel pairs with an iterative mean field approximation of Eq. 2; and *RNN-CRF*, which takes a similar approach to FC-CRF, but it is now end-to-end trainable using Recurrent Neural Networks (RNNs). A visual comparison of the three types of CRF is provided in Fig 4.

4.6.1. Locally Connected CRF

Restricting the pairwise potentials to neighbouring pixels, the resulting CRF is designed to induce local smoothness. [Roth et al. \(2015\)](#) explore 2D CRF as well as a 3D Gaussian smoothing as post-processing for pancreas segmentation in CT images. The weights corresponding to pairwise and unary potentials are calibrated by a grid-search. In terms of performance, the authors evaluate on 82 contrast-enhanced abdominal CT volumes in a 4-fold cross-validation manner, and report an average of 3.3% gain in Dice using CRF that falls short of a 6.9% gain using Gaussian smoothing. However, CRF does reduce the standard deviation of Dice in all experiments, demonstrating its regularization capability in reducing inference variance. [Cai et al. \(2016\)](#) use CRF to fuse mask and boundary predictions, which are separate branches off the same backbone during training, as a cascaded task that post-processes pancreas segmentation of MR Images. In this work, CRF still operates on neighbouring pixels in a feature space spanned by hand-crafted image features and the features learned by both segmentation branches. By using CRF for decision fusion, the authors report a 2.3% gain in Dice ($73.8\% \pm 12.0\% \rightarrow 76.1\% \pm 8.7\%$) over a baseline without CRF on a MRI dataset consisting of 78 scans (52 for training and 26 for testing).

4.6.2. Fully Connected CRF (FC-CRF)

[Krähenbühl and Koltun \(2011\)](#) provides an efficient inference approach to Eq. 2 using mean field approximation. The resulting algorithm reduces the computational complexity from quadratic to linear in the number of pixels involved in the computation. FC-CRF has proven effective as a segmentation

post-processing solution for both natural images [Chen et al. \(2017\)](#) and 2D medical images, e.g. [Fu et al. \(2016b\)](#) in retinal images, [Gao et al. \(2016\)](#) on individual CT slices. The work by [Kamnitsas et al. \(2017\)](#) is the first to extend FC-CRF to 3D brain lesion segmentation in MR Images, leveraging intensity and spatial association under 3D context. However, their 3D generalization on BraTS dataset [Menze et al. \(2014\)](#) (274 training and 110 testing) leads to marginal performance gains in Dice, i.e. 3.7% over Random Forests, 0.3% over an ensemble method, and merely 0.7% over their proposed architecture, which is a patch-based multi-scale 3D CNN network. In addition, the authors note that configuring 3D FC-CRF is a laborious task. Other 3D FC-CRF endeavors include a U-net + 3D FC-CRF by [Christ et al. \(2016\)](#) for liver and lesion segmentation in CT images and a 3D FC-CRF with spectral coordinates characterization by [Wachinger et al. \(2018\)](#) for neuroanatomy segmentation in MR Images. In the works above, FC-CRF refines segmentation masks that often exhibit small isolated regions and zigzag boundaries, but its effectiveness is greatly hindered by the extensive manual tweaking, or in other words, being not end-to-end trainable.

4.6.3. CRF as Recurrent Neural Networks (RNN-CRF)

RNN-CRF organically integrates CRF with CNNs, making it possible to train the whole network in an end-to-end manner. [Zheng et al. \(2015\)](#) reformulates the mean field approximation of FC-CRF as a stack of common CNN layers and the iterative optimization as hidden states in an RNN. [Fu et al. \(2016a\)](#) combine a multi-scale and multi-level CNN that has auxiliary output layers with a RNN-CRF, and achieve the state-of-the-art performance of vessel segmentation on three public fundus datasets (DRIVE, STARE and CHASE-DB1). [Monteiro et al. \(2018\)](#) implement a 3D version of RNN-CRF for volumetric medical images on top of a V-net segmentation network. The authors evaluate their 3D RNN-CRF on multiple datasets. On the PROMISE 2012 dataset, which consists of 50 3D-MRI prostate images, 3D RNN-CRF improves the Dice from $76.7\% \pm 10.9\%$ to $78.0\% \pm 11.0\%$ evaluated in a 5-fold cross-validation manner. And on BraTS 2015 [Menze et al. \(2014\)](#), consisting of 220 multi-modal MR images of brain tumors, 3D RNN-CRF slightly improves the Dice for tumor segmentation from $73.5\% \pm 10.5\%$ to $73.8\% \pm 10.5\%$ based upon a split of 85%/15% (187 training and 33 testing). The authors acknowledge that the improvements by 3D RNN-CRF are inconclusive, and attribute that to the intrinsic differences between natural and medical images: 1) object segmentation in 2D RGB images is generally easier with greater contrast and better defined boundaries; 2) the relatively low resolution of 3D volumes causes a mosaic appearance, which poses further challenges on top of blurry edges; and 3) the local nature of ROIs in medical images downgrades the need to capture global image context beyond what is modeled by the segmentation network, leaving less room for improvement by the CRF. More recently, [Chen and de Bruijne \(2018\)](#) report promising results with their 3D RNN-CRF implementation jointly trained with a 3D U-net for the task of brain lesion segmentation in MR Images. In their approach, CRF operates on high-level features

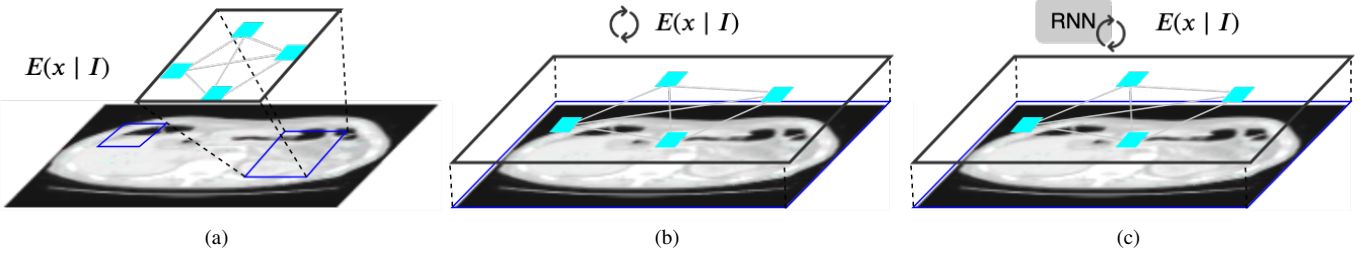


Figure 4: Post segmentation refinement can, to some degree, correct the segmentation errors. (a) local CRF optimizes Gibbs energy over local patches weighing in pairwise pixel dependency. (b) Fully Connected CRF (FC-CRF) extends the local scope of the CRF to the whole image in an efficient manner. (c) CRF as Recurrent Neural Networks (RNN-CRF) makes FC-CRF end-to-end trainable by replacing the iterative calculations with an RNN.

learned by the CNN, which are less prone to image noise than raw intensity values directly taken from the input image. The authors evaluate on 60 MR scans from WMH 2017 Challenge (36 training, 12 validation and 12 testing) and report between six to seven points increase in Dice over a baseline U-Net and other implementations of CRF.

4.6.4. summary

In this section, we reviewed different variants of CRF for the task of post-segmentation refinement. We started with locally connected CRF, which encourages smoothness constraints on local regions of segmentation maps. We then reviewed fully connected CRF, which solves a global optimization problem over the entire segmentation mask. While both locally- and fully-connected CRF have proved effective in 2D segmentation applications, their extension to 3D applications has shown only mixed results. These methods further require extensive parameter tuning and may be susceptible to image noise as they operate directly on pixel information. Finally, we reviewed RNN-CRF, which operates on CNN feature maps and is trained end-to-end along with the segmentation model, thereby addressing the limitations of parameter tuning and susceptibility to image noise.

5. Problem II: Weak Annotations

Creating manual segmentation masks, also known as strong annotations, is time consuming and tedious, particularly for 3D images. To combat the high cost associated with strong annotations, researchers have recently explored the use of weak annotations, which can be obtained at significantly lower annotation cost. Reviewing the literature, we have identified three types of weak annotations: 1) image level annotations; 2) sparse annotations, where only a fraction of the slices or pixels are annotated; and 3) model-generated annotations or noisy annotations, which tend to appear under- and over-segmented. Figure 5 shows different types of weak annotations outlined above. While the absence of strong annotations may seem like an obvious handicap, recent research, as summarized below, has shown that it is possible to train fairly effective models with weak annotations.

5.1. Learning with Image Level Labels

Weakly supervised techniques can take advantage of bounding boxes or image level labels. The common weakly supervised approaches suggested for medical image segmentation are based on class activation maps or multiple instance learning. We review both approaches as follows.

5.1.1. Class Activation Maps (CAMs)

A recurring idea in weakly supervised learning is the use of class activation maps [Zhou et al. \(2016\)](#) and its variants (e.g., [Selvaraju et al. \(2017\)](#)), where the idea is to combine the feature maps to generate class-specific saliency maps. In the following, we review how this technique can be used in conjunction with image-level annotations.

The trend for tackling the problem of having only image-level labels is to use some form of class activation maps (CAMs), which can be binarized to generate a segmentation mask. For the task of diagnostic brain tumor segmentation in confocal laser endomicroscopy (CLE) glioma images, [Izadyazdanabadi et al. \(2018\)](#) use a multi-layer CAM in the form of a 3-stage inception network where the penultimate feature maps from each network are passed on to the next stage. In parallel, CAM followed by global average pooling is applied to these feature maps to obtain the image-level label prediction. The network performance is boosted further by upregulation of confident predictions and downregulation uncertain predictions, wherein the regions activated in a single class map are determined to be confident and those activated in both class maps are uncertain. The dataset consists of 6287 CLE images from 20 patients with a 12-4-4 patient split for training, validation and testing. Their average IOU improvement across different tests over the baseline of just using CAM is 20%. [Feng et al. \(2017\)](#) propose a 2-stage approach consisting of a coarse image segmentation followed by a fine instance-level segmentation. The first stage makes use of CAM via an image classification model, which learns whether a slice has a nodule or not. In the second stage, a region of interest is selected around each localized instance in the class activation map and everything outside this region is masked out. Each masked image is then passed to the same classification network to obtain an instance-level segmentation mask, removing false positive regions produced in stage 1. The authors use the LIDC-IDRI dataset, but convert contour

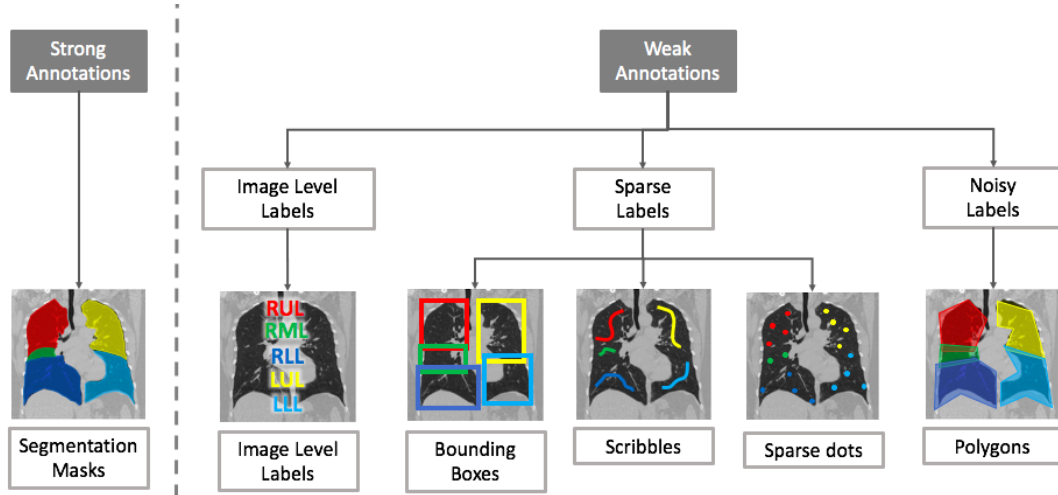


Figure 5: Comparing strong and weak annotations for lung lobes in the coronal view of a chest CT scan. (left) an example of strong annotations in the form of well contoured segmentation masks. (right) examples of different types of weak annotations discussed in this section, which can take the form of (i) bounding box or image level labels, (ii) sparse pixel annotations, or (iii) noisy annotations

annotations to slice-level labels. From 1010 patients, 8345 slices are selected for each class: nodule and non-nodules, and the patients are divided in a 4:1:1 training, validation and testing split. The suggested method achieves a 10% Dice score improvement over the CAM baseline.

5.1.2. Multiple Instance Learning (MIL)

Multiple Instance Learning (MIL) refers to a classification scheme where the labels are provided for each bag of instances rather than each individual instance. If the label is negative, all instances in the bag are negative. However, if the label is positive, then at least one instance in the bag is positive. Since there is no information about which instances in the positive bag are actually positive instances, assigning the bag-level label to each instance in the bag would result in noisy and unreliable labels. In the context of weakly supervised image segmentation, each image can be considered as a bag of instances where each instance can be a pixel or a tile in the image. By learning to classify the image as a whole, MIL learns to predict instance-level predictions, or equivalently the segmentation prediction for the input image.

Jia et al. (2017) use a multiple instance learning approach to generate pixel-level predictions given only image-level cancer labels for histopathology images. The suggested model consists of a VGG network that generates image level classification scores at multiple levels. For this purpose, the authors propose a soft aggregation layer that reduces the feature maps to a cancer classification score. By classifying each image into cancerous and healthy, the authors treat each histopathology image as a bag and each individual pixel in the image as an instance. To regularize training, the authors further impose area constraints (provided during annotation) on segmentation results by MIL. The authors use a histopathology image dataset of colon cancer, consisting of 330 cancer and 580 non-cancer images, of which 250 cancer and 500 non-cancer images are used for training; 80 cancer and 80 non-cancer

images are used for testing. The improvement in F-measure over the baseline (without area constraints and multiple-level predictions) is 6% around the boundaries and 2% overall.

Campanella et al. (2019) train a weakly supervised segmentation model for whole slide histopathology images using only slide-level labels. The slides are divided into small tiles and the multiple instance training procedure includes a full inference pass of the dataset through a CNN, to rank the tiles according to their probability of being positive. The most suspicious tiles in each slide are sequentially passed to an RNN to predict the final slide-level classification, and the heatmaps produced by the RNN are considered as segmentation predictions. The authors use a dataset consisting of 44,732 slides from 15,187 patients across three different tissue types: prostate, skin and axillary lymph nodes. They achieve a 1% increase in AUC when using the RNN classifier over just using the MIL approach directly.

5.1.3. Summary

The papers reviewed in this section address the problem of image segmentation with the weakest form of annotation: image-level labels. Section 5.1.1 delved into the use of CAMs, which generate segmentation masks from intermediate outputs of a classification network. Section 5.1.2, on the other hand, treated this form of weak supervision as a label noise problem that can be solved via MIL. While both approaches improve the model performance over their respective baselines, it would be interesting to see how these two techniques can be combined together to achieve even higher gains.

5.2. Learning with Sparse Labels

Incomplete or sparse annotations refer to annotations where the masks are only provided for a fraction of the slices of a 3D volume, or for only a fraction of the pixels of a 2D image. There are various methods for dealing with these annotations as discussed below. Since the pixels (or voxels)

are only partially labelled, the underlying theme in these methodologies is the use of a selective pixel loss wherein only the labeled pixels contribute to the loss.

5.2.1. Selective Loss with Mask Completion

The papers discussed in this subsection all attempt to artificially reconstruct the incomplete regions of the ground truth masks and use the completed masks for training.

Zhang et al. (2019c) propose a method for brain extraction and brain tissue segmentation in 3D MR images with a sparse set of annotations, where only a fraction of the slices are annotated at irregular intervals. To complete the sparse annotations, the authors use active learning. Specifically, the non-annotated slices are ranked by the Dice similarity coefficient between the output feature maps and attention maps, which are generated by a segmentation network equipped with channel-wise and spatial attention mechanisms. The slices with lowest Dice similarity are then presented to an expert for annotation. The authors evaluate their method on a brain MRI dataset of 40 neonates, but did not discuss their training-testing split, they have instead only shown the effect of incrementally utilizing the training set in an active learning framework. For the task of brain extraction, the suggested method trained with just 15% of the slices labeled yields results similar to that of a model trained with a 50% annotation rate. For brain tissue segmentation, the model requires 30% of slices to be labeled in order to achieve a similar level of performance. In addition to having spatially sparse annotations, when dealing with time sequence data, the annotations may be temporally sparse. Bai et al. (2018) propose an image sequence segmentation algorithm by combining a fully convolutional network with a recurrent neural network, which incorporates both spatial and temporal information into the segmentation task. The missing annotations are then recovered through a non-rigid label propagation scheme. The authors use an aortic MR image set of 500 subjects, with 400 subjects used for training and the remaining 100 for testing. The model trained using the additional masks recovered for unlabeled time frames achieves 1% improvement in Dice over the U-Net baseline that was only trained on labeled time frames.

Cai et al. (2018) train a 3D segmentation model using only 2D annotations, which consist of diameter markings along the short and long axes of each lesion on the slice where the lesion appears the largest. The authors first refine the initial ground truth markings through the application of GrabCut. The suggested method then alternates between two steps. The first step consists of training the model using augmented ground truth masks. The second step expands the ground truth masks by running the trained model on the non-annotated slices adjacent to the annotated slices followed by applying GrabCut on the generated masks. This iterative process continues until all slices that contain a lesion are annotated. The authors make use of the DeepLesion dataset which is composed of 32,735 bookmarked CT lesion instances, of which 28,000 lesion volumes are used for training and the rest for testing. This method achieves 10% improvement in Dice over a model trained using the original diameter markings.

Scribbles have been recognized as a user-friendly alternative to overlapping bounding boxes. To generate the initial ground truth, Can et al. (2018) use a random walk image segmentation approach with a high threshold to perform region growing around seed scribble annotations. Once the initial masks are generated, they suggest an iterative framework to incrementally refine the segmentation masks. Each iteration consists of two stages: 1) training the segmentation network with a CRF-RNN layer using the current annotations, 2) using test time dropout to make multiple predictions for each image and assess the uncertainty of each pixel-level prediction in the image. The new ground truth in each iteration is comprised of only the certain predictions. The authors make use of 2 datasets: 1) the ACDC cardiac segmentation challenge data, split into 160 training and 40 validation volumes, and an additional 100 images for evaluating the model using the challenge server, and 2) the NCI-ISBI 2013 prostate segmentation challenge containing 29 volumes split into 12 training, 7 validation and 10 testing volumes. They achieve a 3% average Dice improvement over their non-iterative baseline.

Matuszewski and Sintorn (2018) perform virus segmentation in electron microscopy images given minimal manual annotation in the form of points or lines. They artificially construct the ground truth masks by dilating the manual annotations with disc shaped structural elements, using a smaller disc for creating the foreground and a larger disc for creating the inverted background. Due to the different sized structural elements used, there exists unlabeled pixels at the boundary of the foreground and background that do not contribute to the segmentation loss while training. The authors use the Rift Valley virus dataset containing 143 images with 95 used for training and the remaining 48 for testing. They show a 7% increase in Dice when using this scheme, over an approach where all pixels contribute to the loss and undefined boundary regions are penalized. However, no comparison was made against a fully-supervised oracle or other state-of-the-art weakly supervised approaches.

5.2.2. Selective Loss without Mask Completion

Reconstructing the complete segmentation mask is not always a requirement. The papers reviewed below circumvent ground truth completion by modifying the objective function. Silvestri and Antiga (2018) recommend using a hexagonal grid for sparse annotations and show that a dense mask is not a requirement for training an effective pancreas segmentation model for abdominal CT scans. They compare using grids of different strides and the effect of padding the grid points to generate the training masks. The padding process consists of extending the ground truth masks around the sparse points to form discrete label blocks, but does not attempt to complete the segmentation masks. The authors use a dataset containing 399 high-resolution abdominal CT scans, of which 79 scans are used for testing and the rest for training. Their results show that using a grid stride of 9 pixels achieve a comparable performance to using a grid size of 3 pixels. The higher the stride, the fewer grid points that need to be annotated. Çiçek et al. (2016) train a 3D model to segment kidney tubules in 3D

confocal microscopy images using only sparse annotations. They propose using an additional class for unlabeled pixels. For annotated slices, the segmentation loss is class-balanced cross entropy where only the labeled pixels contributed to loss. Using a dataset of three samples of *Xenopus* kidney embryos and a 3-fold cross-validation scheme, the authors demonstrate a significant gain in IoU (0.4→0.86) when the annotation rate increases from 2.5% to just 8.9%.

Bokhorst et al. (2018) compare 2 different class-balancing methods that can be used to improve the segmentation performance given sparse annotations without trying to fill in the missing mask pixels. In the suggested method, only the labeled pixels contribute to a weighted segmentation loss. The loss-weighting to balance the classes is performed at the instance level or mini-batch level. Their dataset of whole slide images (WSI) contained 43 WSIs with sparse annotations and 8 with dense annotations in the training set, 11 WSIs with sparse annotations and 2 with dense annotations in the validation set and a test set containing 5 WSIs with only dense annotations. The authors show that using instance-based balancing improves the Dice score by 1% and mini-batch balancing improves it by 4% when trained entirely on sparsely annotated images. Zhu et al. (2019) introduce a new quality awareness module (QAM), which is a CNN trained in parallel with the segmentation network to assess the quality of the masks. QAM uses the image with its mask as input and computes a new loss-weight for each sample in the mini-batch to ensure that the new segmentation loss penalizes different images differently based on the quality of the mask as measured by the secondary network. The authors use the JSRT dataset containing 247 X-ray images with segmentation masks for three types of organ structures: heart, clavicles, and lungs. They split the dataset with 165 training and 82 testing images. They artificially create noisy labels by eroding and dilating them with different sizes of structural elements. Their results show that as the level of label noise increases, the baseline segmentation model starts to perform significantly worse, but their model with QAM-weighted segmentation loss retains its high accuracy.

5.2.3. Summary

The papers covered in this section deal with incomplete pixel labels and follow one of two distinct schools of thought: those that attempt to artificially complete the labels for the unlabeled pixels (Section 5.2.1) and those that do not (Section 5.2.2). The former tends to be iterative, making these methods slow to train yet fairly reliable, because only confidently labeled pixels are added to the set of labeled pixels in each iteration. The latter, on the other hand, is more straightforward to implement, because it uses only the available labeled pixels with proper loss-weighting schemes. Although there is no direct comparison between the two approaches, we surmise that the approaches attempting to create pseudo ground truth masks will benefit from better gradient flow through larger portions of the image.

5.3. Learning with Noisy Labels

Noisy labels for the task of image segmentation refer to ambiguities or inaccuracies in the boundaries of the segmentation masks. For medical images in particular, label noise could be induced by annotators unintentionally (random errors), or by inconsistencies between different readers due to human subjectivity concerning ambiguous lesions (expertise errors) Gu et al. (2018). This type of annotation noise can be simulated by representing the labels as a polygon and then reducing the number of polygon vertices, which has the effect of creating segmentation error in the peripheral areas of segmentation masks. Label noise could also arise in semi-supervised learning with pseudo annotations (Section 4.4.2) where the model learns from its own predictions on unlabeled data. Label noise, if left untreated, can degrade the performance of the segmentation model. It is therefore important to utilize strategies that mitigate the adverse effects of label noise during training.

5.3.1. Robust Loss without Mask Refinement

Mirikharaji et al. (2019) propose a learning algorithm resilient to the label noise in the segmentation masks. The suggested method consists of a weighted cross entropy loss function where the contribution of each pixel to the total loss is controlled by model's perception of the annotation quality for the pixels. During training, the weight matrices are updated based on the batches of images with clean annotations, and then used to scale the segmentation loss at the pixel-level for batches with noisy annotations. The authors simulate the annotation noise by replacing the segmentation masks with polygons of varying number of vertices. For the task of skin lesion segmentation, the authors use a skin image dataset consisting of 2000 training, 150 validation and 600 test images with their corresponding segmentation masks, and show that a model trained using the suggested loss and 3-vertex polygon masks performs comparably to the model trained using full annotation masks.

5.3.2. Robust Loss with Iterative Mask Refinement

A proper handling of label noise is also studied in the context of semi-supervised learning with pseudo annotations where the model-generated annotations, commonly corrupted by noise, are used to fine-tune the model in an iterative manner. The common solution in this context is to identify samples with noisy labels during training and then lower their impact on parameter updates by downplaying their gradients. In doing so, the model becomes capable of predicting more accurate labels for unlabeled data. The labeled data and pseudo-annotated unlabeled data are then used to improve the model and this process can be repeated as needed. Min et al. (2018) propose a two stream network with independent weights whose concord determine the quality of segmentation mask. Nie et al. (2018) propose a segmentation network with adversarial loss where the job of the discriminator network is to identify the reliable annotated regions from noisy annotations. Readers can refer to Section 4.4.2 for a detailed discussion of these approaches.

5.3.3. Summary

Similar to the methods for handling sparse labels (Section 5.2), the papers reviewed in this section either attempt to refine the noisy masks (Section 5.3.2) or leave them as is (Section 5.3.1). However, they differ from the sparse label techniques in that the pixels that contribute to the loss are not predefined but decided on the fly. The former approaches are iterative and slow to train, reducing the adverse effects of label noise on the segmentation model to a minimum. The latter approaches, on the other hand, are more straightforward to implement, because they use various loss-weighting schemes.

6. Discussion

In Figure 1, we split the data limitations into scarce annotations and weak annotations, which allowed us to group similar methodologies with ease. However, when making use of multiple datasets, it is possible that the combined dataset now suffers from both scarce and weak annotations. A combination of each individual solution can be used in tackling such datasets. For example, if a small dataset of histopathology images had tumor segmentation masks available, but another much larger histopathology image dataset had only image level tumor classification labels available, then a multi-task framework incorporating a semi supervised approach like Sedai et al. (2017) used in conjunction with a CAM-based approach like Feng et al. (2017) could address the issue of both scarce annotations and weak annotations while utilizing the joint potential of this new larger dataset. When faced with the task of annotating a large dataset with a limited budget, it may also be helpful to get a small subset with dense segmentation mask annotations and only weak annotations for the remaining subset and use a combined strategy to train a robust model.

Table 7 presents a summary of the methodologies suggested for the problems of scarce and weak annotations. For clarity, the table is split into two sections, each focusing on one annotation problem. We have further grouped the methodologies in each section by the general and specific strategies the follow. Color encoding is also used to indicate the data requirements of each methodology. We hope this table can serve as a strategy guideline, assisting the readers in choosing the right methodology according to the dataset problems they face and the data resources they have available. In what follows, we highlight the important messages of Table 7.

As indicated by the color encoding, the methodologies suggested for the problem of scarce annotations can be placed in three broad categories according to the data requirements:

1. *Solutions with low data requirements:* This group of solutions rely solely on the available labeled segmentation dataset, requiring no additional labeled or unlabeled training data. Therefore, they should be utilized wherever possible. Of the suggested methodologies, CRF-based post-processing has shown mixed results for 3D segmentation, and altered 3D image representations have achieved medium gains at the price of training several 2D models. Therefore, in

addition to traditional data augmentation, which is the de facto solution to the scarce annotation problem, we recommend using shape regularization, data augmentation by mixing images, and same-domain data synthesis for both 2D and 3D applications, and CRF-based post-processing for 2D applications.

2. *Solutions with medium data requirements:* This set of methodologies requires access to additional labeled or unlabeled training data from the same or a similar domain. Therefore, depending on the application at hand and the availability of the corresponding auxiliary datasets, these solutions may or may not be applicable. Of the suggested methodologies, semi-supervised learning with pseudo annotations has shown mixed results with the exceptions being methods that adopt advanced architectures to handle annotation noise in model-generated annotations. Domain adaptation techniques are effective, but they can be difficult to adopt due to the instability of adversarial training, which lies at the core of these methodologies. Semi-supervised learning without pseudo annotations require only additional unlabeled data and are typically less demanding to implement compared to unsupervised domain adaptation methods. Multi-task learning and dataset fusions are both straightforward solutions with reasonable performance gains. In our opinion, self-supervised pre-training is one of the most promising approaches in this category, requiring only unlabeled data and typically only minor modifications to the architecture.
3. *Solutions with high data requirements:* These solutions require access to medical experts, but their elegance lies in the use of expert knowledge in a cost-effective manner. Two solutions in this category are active learning and interactive segmentation where the former determines which samples to be annotated by experts whereas the latter helps experts complete the annotation tasks quickly. If our hands are forced into annotating more data or if additional data annotation is deemed highly advantageous, then these two methodologies should be prioritized in practice.

The methodologies suggested for handling weak annotations are closely related to the types of annotations that are readily available for training. For each type, we compare and recommend methodologies that best suit the given limitation from the perspectives of performance gains and annotation cost.

1. *Noisy annotations:* A common problem with medical datasets and in particular segmentation datasets is annotation noise where the annotated contours may not always follow the contours of the region of interest. Handling annotation noise is important, because not only does it reduce the adverse effects of inter-observer annotation variability on the trained model, but it also enables training with only rough annotations, which can

Table 7: Top-down overview of the methodologies suggested for the problems of scarce and weak annotations, where the methodologies are grouped by the underlying general and specific strategies. We have further used color encoding to show the required data resources of each methodology. Methodologies highlighted in green require no further data resources in addition to the original limited annotated dataset available for training; thus, they should be used wherever possible. Methodologies highlighted in orange require access to additional unlabeled data from the same domain or labeled data from a similar domain. Methodologies highlighted in red require experts in the loop; and thus, may not always be a viable option.

Problem I: Scarce Annotations			
General Strategy	Specific Strategy	Methodology	Description
Expanding the dataset	Augmenting the limited data with new artificial examples	Same-domain data synthesis	Training a segmentation model with additional labeled data generated by an image synthesis model
		Data augmentation by mixing images	Training a segmentation model with additional labeled data generated by blending the labeled images
		Traditional data augmentation	Training a segmentation model with additional labeled data generated by spatial and intensity transformation
	Leveraging additional unlabeled data from the same domain	Semi-supervised learning with pseudo labels	Annotating unlabeled images using models' own predictions and then using the augmented dataset for training a segmentation model
		Semi-supervised learning without pseudo labels	Training a segmentation model with both labeled and unlabeled data
		Self-supervised pre-training	Pre-training a model using unlabeled medical data and then fine-tuning the model for the target segmentation task
	Leveraging external labeled data from a similar domain	Transfer learning	Training a segmentation model from the knowledge learned from natural images (ImageNet or COCO)
		Dataset fusion	Training a universal segmentation model from heterogeneous datasets by learning to discriminate between the datasets
		Domain adaptation w/ target labels	Training a segmentation model using shared feature representations learned across multiple domains
		Domain adaptation w/o target labels	Training a segmentation model using only source domain labels by translating from one domain to the other
	Collecting additional annotations with experts in the loop	Active learning	Selecting unlabeled images for annotation judiciously based on model predictions
		Interactive segmentation	Accelerating the annotation process by propagating the user changes throughout the segmentation mask
Training w/ regularization	Leveraging additional tasks	Multi-task learning	Training a segmentation model with additional heads, each for a separate classification task
	Imposing additional constraints	Shape regularization	Training a segmentation model by imposing shape constraints on predicted segmentation masks
	Leveraging more informative or compressed input data	Altered image representation	Training a segmentation model with a more compact or informative image representation
Post-training refinement	Using post-processing methods to refine segmentations	CRF-based post segmentation	Using CRF as a post-processing or as a trainable module in the segmentation network
Problem II: Weak Annotations			
Leveraging weak annotations	Learning with sparse annotations	Selective loss w/ and w/o mask completion	Training a segmentation model by excluding unannotated pixels from backpropagation
	Learning with noisy annotations	Robust loss w/ and w/o iterative label refinement	Training a segmentation model with mechanisms that downgrade unreliable annotations during training
	Learning with image-level annotations	Class activation maps	Training a classification model with global average pooling and using activation maps as class-specific segmentation
		Multiple instance learning	Training a classification model with aggregation layers and using activation maps as class-specific segmentation

be obtained in a cost-effective manner with significantly shorter annotation time than that of accurate annotations. For instance, the work by [Mirikharaji et al. \(2019\)](#) shows that, with a noise-resilient approach, a skin segmentation model trained with 3-vertex contours can achieve similar performance to a model trained using accurate segmentation masks. Handling annotation noise in medical segmentation datasets is still a fairly new topic and deserves further investigation.

2. *Sparse annotations:* Of the weakly supervised approaches reviewed, the papers tackling sparse annotation have achieved the closest performance to their strongly supervised counterparts; however, the application of sparse annotations may not always be viable. For instance, while dot grids [Silvestri and Antiga \(2018\)](#) may be useful for larger organ segmentation, they would not be as effective for segmenting small lesions. Furthermore, even though sparse annotations are easier to obtain than strong segmentation masks, the annotation process is still not entirely user-friendly, and the training schemes tend to be iterative, leading to

longer training periods.

3. *Image-level annotations:* Of the weak annotations reviewed, image-level annotation incur the least annotation cost. Comparing the suggested methodologies, we would recommend using the modified CAM-based approaches with image level-labels. Not only do they use the least expensive form of annotation, but they also show large improvement in Dice over the direct CAM approaches and only fall a couple of Dice points short of using full supervision with strong annotations [Feng et al. \(2017\)](#).

7. Conclusion

In this survey, we covered data limitations associated with medical image segmentation datasets, namely, scarce annotations and weak annotations. For the problem of scarce annotations, we reviewed a diverse set of solutions, ranging from semi-automated solutions that require human experts in the loop such as active learning and interactive segmentation, to fully-automated solutions that leverage unlabeled and

synthetic data from the same domain or labeled data from similar domains. For the problem of weak annotations, we studied solutions with the capability of handling sparse, noisy, or only image-level annotations. We further compared the suggested methodologies in terms of required data resources, difficulty of implementation, and performance gains, highlighting methodologies with the best cost-gain trade-off. We hope this survey increases the community awareness of the strategies for handling scarce and weak annotations in medical image segmentation datasets, and further inspires efforts in this impactful area of research.

8. Acknowledgment

We would like to thank Ju Hu for helping us with compiling the list of related works in the initial stage of this research.

References

- Abhishek, K., Hamarneh, G., 2019. Mask2lesion: Mask-constrained adversarial skin lesion image synthesis, in: Burgos, N., Gooya, A., Svoboda, D. (Eds.), *Simulation and Synthesis in Medical Imaging*, Springer International Publishing, pp. 71–80.
- Agustsson, E., Timofte, R., 2017. Ntire 2017 challenge on single image super-resolution: Dataset and study, in: *The IEEE Conference on Computer Vision and Pattern Recognition (CVPR) Workshops*.
- Alex, V., Vaidhya, K., Thirunavukkarasu, S., Kesavadas, C., Krishnamurthi, G., 2017. Semisupervised learning using denoising autoencoders for brain lesion detection and segmentation. *Journal of Medical Imaging* 4, 041311.
- Alom, M.Z., Hasan, M., Yakopcic, C., Taha, T.M., Asari, V.K., 2018. Recurrent residual convolutional neural network based on u-net (r2u-net) for medical image segmentation. *arXiv preprint arXiv:1802.06955*.
- Angermann, C., Haltmeier, M., Steiger, R., Pereverzyev Jr, S., Gizewski, E., 2019. Projection-based 2.5 d u-net architecture for fast volumetric segmentation. *arXiv preprint arXiv:1902.00347*.
- Bai, W., Chen, C., Tarroni, G., Duan, J., Guitton, F., Petersen, S.E., Guo, Y., Matthews, P.M., Rueckert, D., 2019. Self-supervised learning for cardiac mr image segmentation by anatomical position prediction. *arXiv preprint arXiv:1907.02757*.
- Bai, W., Oktay, O., Sinclair, M., Suzuki, H., Rajchl, M., Tarroni, G., Glocker, B., King, A., Matthews, P.M., Rueckert, D., 2017. Semi-supervised learning for network-based cardiac mr image segmentation, in: *International Conference on Medical Image Computing and Computer-Assisted Intervention*, Springer, pp. 253–260.
- Bai, W., Suzuki, H., Qin, C., Tarroni, G., Oktay, O., Matthews, P.M., Rueckert, D., 2018. Recurrent neural networks for aortic image sequence segmentation with sparse annotations, in: *International Conference on Medical Image Computing and Computer-Assisted Intervention*, Springer, pp. 586–594.
- Baur, C., Albarqouni, S., Navab, N., 2017. Semi-supervised deep learning for fully convolutional networks, in: *International Conference on Medical Image Computing and Computer-Assisted Intervention*, Springer, pp. 311–319.
- Bokhorst, J.M., Pinckaers, H., van Zwam, P., Nagtegaal, I., van der Laak, J., Ciompi, F., 2018. Learning from sparsely annotated data for semantic segmentation in histopathology images.
- Bortsova, G., Dubost, F., Hogeweg, L., Katramados, I., de Bruijne, M., 2019. Semi-supervised medical image segmentation via learning consistency under transformations, in: *International Conference on Medical Image Computing and Computer-Assisted Intervention*, Springer, pp. 810–818.
- Boykov, Y.Y., Jolly, M.P., 2001. Interactive graph cuts for optimal boundary & region segmentation of objects in nd images, in: *Proceedings eighth IEEE international conference on computer vision. ICCV 2001*, IEEE, pp. 105–112.
- Cai, J., Lu, L., Zhang, Z., Xing, F., Yang, L., Yin, Q., 2016. Pancreas segmentation in mri using graph-based decision fusion on convolutional neural networks, in: *International Conference on Medical Image Computing and Computer-Assisted Intervention*, Springer, pp. 442–450.
- Cai, J., Tang, Y., Lu, L., Harrison, A.P., Yan, K., Xiao, J., Yang, L., Summers, R.M., 2018. Accurate weakly supervised deep lesion segmentation on ct scans: Self-paced 3d mask generation from recist. *arXiv preprint arXiv:1801.08614*.
- Campanella, G., Hanna, M.G., Geneslaw, L., Miraflor, A., Werneck Krauss Silva, V., Busam, K.J., Brogi, E., Reuter, V.E., Klimstra, D.S., Fuchs, T.J., 2019. Clinical-grade computational pathology using weakly supervised deep learning on whole slide images. *Nature Medicine* URL: <https://doi.org/10.1038/s41591-019-0508-1>, doi:10.1038/s41591-019-0508-1.
- Can, Y.B., Chaitanya, K., Mustafa, B., Koch, L.M., Konukoglu, E., Baumgartner, C.F., 2018. Learning to segment medical images with scribble-supervision alone, in: *Deep Learning in Medical Image Analysis and Multimodal Learning for Clinical Decision Support*. Springer, pp. 236–244.
- Chaitanya, K., Karani, N., Baumgartner, C.F., Becker, A., Donati, O., Konukoglu, E., 2019. Semi-supervised and task-driven data augmentation, in: *International Conference on Information Processing in Medical Imaging*, Springer, pp. 29–41.
- Chartsias, A., Joyce, T., Dharmakumar, R., Tsafaris, S.A., 2017. Adversarial image synthesis for unpaired multi-modal cardiac data, in: *International Workshop on Simulation and Synthesis in Medical Imaging*, Springer, pp. 3–13.
- Chartsias, A., Joyce, T., Papanastasiou, G., Semple, S., Williams, M., Newby, D., Dharmakumar, R., Tsafaris, S.A., 2018. Factorised spatial representation learning: application in semi-supervised myocardial segmentation, in: *International Conference on Medical Image Computing and Computer-Assisted Intervention*, Springer, pp. 490–498.
- Chen, C., Dou, Q., Chen, H., Heng, P.A., 2018. Semantic-aware generative adversarial nets for unsupervised domain adaptation in chest x-ray segmentation, in: *International Workshop on Machine Learning in Medical Imaging*, Springer, pp. 143–151.
- Chen, C., Dou, Q., Chen, H., Qin, J., Heng, P.A., 2019a. Synergistic image and feature adaptation: Towards cross-modality domain adaptation for medical image segmentation. *arXiv preprint arXiv:1901.08211*.
- Chen, C., Ouyang, C., Tarroni, G., Schlemper, J., Qiu, H., Bai, W., Rueckert, D., 2019b. Unsupervised multi-modal style transfer for cardiac mr segmentation. *arXiv preprint arXiv:1908.07344*.
- Chen, L.C., Papandreou, G., Kokkinos, I., Murphy, K., Yuille, A.L., 2017. Deeplab: Semantic image segmentation with deep convolutional nets, atrous convolution, and fully connected crfs. *IEEE transactions on pattern analysis and machine intelligence* 40, 834–848.
- Chen, S., Bortsova, G., Juárez, A.G.U., van Tulder, G., de Bruijne, M., 2019c. Multi-task attention-based semi-supervised learning for medical image segmentation, in: *International Conference on Medical Image Computing and Computer-Assisted Intervention*, Springer, pp. 457–465.
- Chen, S., de Bruijne, M., 2018. An end-to-end approach to semantic segmentation with 3d cnn and posterior-crf in medical images. *arXiv preprint arXiv:1811.03549*.
- Cheplygina, V., de Bruijne, M., Pluim, J.P., 2019. Not-so-supervised: a survey of semi-supervised, multi-instance, and transfer learning in medical image analysis. *Medical Image Analysis*.
- Christ, P.F., Elshaer, M.E.A., Ettlinger, F., Tatavarty, S., Bickel, M., Bilic, P., Rempfler, M., Armbruster, M., Hofmann, F., D’Anastasi, M., et al., 2016. Automatic liver and lesion segmentation in ct using cascaded fully convolutional neural networks and 3d conditional random fields, in: *International Conference on Medical Image Computing and Computer-Assisted Intervention*, Springer, pp. 415–423.
- Çiçek, Ö., Abdulkadir, A., Lienkamp, S.S., Brox, T., Ronneberger, O., 2016. 3d u-net: learning dense volumetric segmentation from sparse annotation, in: *International conference on medical image computing and computer-assisted intervention*, Springer, pp. 424–432.
- Cohen, T., Welling, M., 2016. Group equivariant convolutional networks, in: *International conference on machine learning*, pp. 2990–2999.
- Cui, W., Liu, Y., Li, Y., Guo, M., Li, Y., Li, X., Wang, T., Zeng, X., Ye, C., 2019. Semi-supervised brain lesion segmentation with an adapted mean teacher model, in: *International Conference on Information Processing in Medical Imaging*, Springer, pp. 554–565.
- Dalca, A.V., Guttat, J., Sabuncu, M.R., 2018. Anatomical priors in convolutional networks for unsupervised biomedical segmentation, in: *Proceedings of the IEEE Conference on Computer Vision and Pattern Recognition*, pp. 9290–9299.

- Dmitriev, K., Kaufman, A.E., 2019. Learning multi-class segmentations from single-class datasets, in: *Proceedings of the IEEE Conference on Computer Vision and Pattern Recognition*, pp. 9501–9511.
- Dong, H., Yang, G., Liu, F., Mo, Y., Guo, Y., 2017. Automatic brain tumor detection and segmentation using u-net based fully convolutional networks, in: *annual conference on medical image understanding and analysis*, Springer. pp. 506–517.
- Dou, Q., Ouyang, C., Chen, C., Chen, H., Glocker, B., Zhuang, X., Heng, P.A., 2018. Pnp-adanet: Plug-and-play adversarial domain adaptation network with a benchmark at cross-modality cardiac segmentation. *arXiv preprint arXiv:1812.07907*.
- Duan, J., Bello, G., Schlemper, J., Bai, W., Dawes, T.J., Biffi, C., de Marvao, A., Doumou, G., O'Regan, D.P., Rueckert, D., 2019. Automatic 3d bi-ventricular segmentation of cardiac images by a shape-refined multi-task deep learning approach. *IEEE transactions on medical imaging*.
- Feng, X., Yang, J., Laine, A.F., Angelini, E.D., 2017. Discriminative localization in cnns for weakly-supervised segmentation of pulmonary nodules, in: *International Conference on Medical Image Computing and Computer-Assisted Intervention*, Springer. pp. 568–576.
- Fu, C., Ho, D.J., Han, S., Salama, P., Dunn, K.W., Delp, E.J., 2017. Nuclei segmentation of fluorescence microscopy images using convolutional neural networks, in: *2017 IEEE 14th International Symposium on Biomedical Imaging (ISBI 2017)*, IEEE. pp. 704–708.
- Fu, C., Lee, S., Joon Ho, D., Han, S., Salama, P., Dunn, K.W., Delp, E.J., 2018a. Three dimensional fluorescence microscopy image synthesis and segmentation, in: *Proceedings of the IEEE Conference on Computer Vision and Pattern Recognition Workshops*, pp. 2221–2229.
- Fu, H., Cheng, J., Xu, Y., Wong, D.W.K., Liu, J., Cao, X., 2018b. Joint optic disc and cup segmentation based on multi-label deep network and polar transformation. *IEEE transactions on medical imaging* 37, 1597–1605.
- Fu, H., Xu, Y., Lin, S., Wong, D.W.K., Liu, J., 2016a. Deepvessel: Retinal vessel segmentation via deep learning and conditional random field, in: *International conference on medical image computing and computer-assisted intervention*, Springer. pp. 132–139.
- Fu, H., Xu, Y., Wong, D.W.K., Liu, J., 2016b. Retinal vessel segmentation via deep learning network and fully-connected conditional random fields, in: *2016 IEEE 13th international symposium on biomedical imaging (ISBI)*, IEEE. pp. 698–701.
- Gal, Y., Ghahramani, Z., 2016. Dropout as a bayesian approximation: Representing model uncertainty in deep learning, in: *international conference on machine learning*, pp. 1050–1059.
- Gao, M., Xu, Z., Lu, L., Wu, A., Nogues, I., Summers, R.M., Mollura, D.J., 2016. Segmentation label propagation using deep convolutional neural networks and dense conditional random field, in: *2016 IEEE 13th International Symposium on Biomedical Imaging (ISBI)*, IEEE. pp. 1265–1268.
- Ghafoorian, M., Karssemeijer, N., Heskes, T., van Uden, I.W., Sanchez, C.I., Litjens, G., de Leeuw, F.E., van Ginneken, B., Marchiori, E., Platel, B., 2017. Location sensitive deep convolutional neural networks for segmentation of white matter hyperintensities. *Scientific Reports* 7, 5110.
- Giger, M.L., 2018. Whole Brain Segmentation and Labeling from CT Using Synthetic MR Images. *Journal of the American College of Radiology* 15, 512–520. doi:10.1016/j.jacr.2017.12.028.
- Gildenblat, J., Klaiman, E., 2019. Self-supervised similarity learning for digital pathology. *arXiv preprint arXiv:1905.08139*.
- Goodfellow, I., Pouget-Abadie, J., Mirza, M., Xu, B., Warde-Farley, D., Ozair, S., Courville, A., Bengio, Y., 2014. Generative adversarial nets, in: *Advances in neural information processing systems*, pp. 2672–2680.
- Gorritz, M., Carlier, A., Faure, E., Giro-i Nieto, X., 2017. Cost-effective active learning for melanoma segmentation. *arXiv preprint arXiv:1711.09168*.
- Gu, Y., Member, S., Yang, J., Yang, G.z., 2018. Reliable Label-Efficient Learning for Biomedical Image Recognition 9294, 1–11. doi:10.1109/TBME.2018.2889915.
- Guibas, J.T., Virdi, T.S., Li, P.S., 2017. Synthetic medical images from dual generative adversarial networks. *arXiv preprint arXiv:1709.01872*.
- Gupta, S., Hoffman, J., Malik, J., 2016. Cross modal distillation for supervision transfer, in: *Proceedings of the IEEE conference on computer vision and pattern recognition*, pp. 2827–2836.
- Harouni, A., Karargyris, A., Negahdar, M., Beymer, D., Syeda-Mahmood, T., 2018a. Universal multi-modal deep network for classification and segmentation of medical images. *Proceedings - International Symposium on Biomedical Imaging 2018-April*, 872–876. doi:10.1109/ISBI.2018.8363710.
- Harouni, A., Karargyris, A., Negahdar, M., Beymer, D., Syeda-Mahmood, T., 2018b. Universal multi-modal deep network for classification and segmentation of medical images, in: *2018 IEEE 15th International Symposium on Biomedical Imaging (ISBI 2018)*, pp. 872–876. doi:10.1109/ISBI.2018.8363710.
- He, K., Gkioxari, G., Dollr, P., Girshick, R., 2017. Mask R-CNN. *arXiv:1703.06870 [cs]* URL: <http://arxiv.org/abs/1703.06870>. *arXiv: 1703.06870*.
- He, Y., Yang, G., Chen, Y., Kong, Y., Wu, J., Tang, L., Zhu, X., Dillenseger, J.L., Shao, P., Zhang, S., et al., 2019. Dpa-densebiasnet: Semi-supervised 3d fine renal artery segmentation with dense biased network and deep priori anatomy, in: *International Conference on Medical Image Computing and Computer-Assisted Intervention*, Springer. pp. 139–147.
- Hesamian, M.H., Jia, W., He, X., Kennedy, P., 2019. Deep learning techniques for medical image segmentation: Achievements and challenges. *Journal of digital imaging*, 1–15.
- Huang, X., Liu, M.Y., Belongie, S., Kautz, J., 2018a. Multimodal unsupervised image-to-image translation, in: *Proceedings of the European Conference on Computer Vision (ECCV)*, pp. 172–189.
- Huang, Y.J., Dou, Q., Wang, Z.X., Liu, L.Z., Jin, Y., Li, C.F., Wang, L., Chen, H., Xu, R.H., 2018b. 3d RoI-aware U-Net for Accurate and Efficient Colorectal Tumor Segmentation. *arXiv:1806.10342 [cs]* URL: <http://arxiv.org/abs/1806.10342>. *arXiv: 1806.10342*.
- Huo, Y., Xu, Z., Bao, S., Assad, A., Abramson, R.G., Landman, B.A., 2018a. Adversarial synthesis learning enables segmentation without target modality ground truth, in: *2018 IEEE 15th International Symposium on Biomedical Imaging (ISBI 2018)*, IEEE. pp. 1217–1220.
- Huo, Y., Xu, Z., Moon, H., Bao, S., Assad, A., Moyo, T.K., Savona, M.R., Abramson, R.G., Landman, B.A., 2018b. Synseg-net: Synthetic segmentation without target modality ground truth. *IEEE transactions on medical imaging* 38, 1016–1025.
- Izadyazdanabadi, M., Belykh, E., Cavallo, C., Zhao, X., Gandhi, S., Moreira, L.B., Eschbacher, J., Nakaji, P., Preul, M.C., Yang, Y., 2018. Weakly-supervised learning-based feature localization for confocal laser endomicroscopy glioma images, in: *International Conference on Medical Image Computing and Computer-Assisted Intervention*, Springer. pp. 300–308.
- Jaeger, P.F., Kohl, S.A.A., Bickelhaupt, S., Isensee, F., Kuder, T.A., Schlemmer, H.P., Maier-Hein, K.H., 2018. Retina U-Net: Embarrassingly Simple Exploitation of Segmentation Supervision for Medical Object Detection. *arXiv:1811.08661 [cs]* URL: <http://arxiv.org/abs/1811.08661>. *arXiv: 1811.08661*.
- Jamaludin, A., Kadir, T., Zisserman, A., 2017. Self-supervised learning for spinal mris, in: *Deep Learning in Medical Image Analysis and Multimodal Learning for Clinical Decision Support*. Springer, pp. 294–302.
- Jia, Z., Huang, X., Eric, I., Chang, C., Xu, Y., 2017. Constrained deep weak supervision for histopathology image segmentation. *IEEE transactions on medical imaging* 36, 2376–2388.
- Jin, D., Xu, Z., Tang, Y., Harrison, A.P., Mollura, D.J., 2018. Ct-realistic lung nodule simulation from 3d conditional generative adversarial networks for robust lung segmentation, in: *International Conference on Medical Image Computing and Computer-Assisted Intervention*, Springer. pp. 732–740.
- Jung, W., Park, S., Jung, K.H., Hwang, S.I., 2019. Prostate cancer segmentation using manifold mixup u-net.
- Kamnitsas, K., Ledig, C., Newcombe, V.F., Simpson, J.P., Kane, A.D., Menon, D.K., Rueckert, D., Glocker, B., 2017. Efficient multi-scale 3d cnn with fully connected crf for accurate brain lesion segmentation. *Medical image analysis* 36, 61–78.
- Karimi, D., Dou, H., Warfield, S.K., Gholipour, A., 2019. Deep learning with noisy labels: exploring techniques and remedies in medical image analysis. *arXiv preprint arXiv:1912.02911*.
- Karimi, D., Salcudean, S.E., 2019. Reducing the hausdorff distance in medical image segmentation with convolutional neural networks. *arXiv preprint arXiv:1904.10030*.
- Kendall, A., Gal, Y., 2017. What uncertainties do we need in bayesian deep learning for computer vision?, in: *Advances in neural information processing systems*, pp. 5574–5584.
- Kervadec, H., Bouchtiba, J., Desrosiers, C., Granger, E., Dolz, J., Ayed, I.B., 2019. Boundary loss for highly unbalanced segmentation, in: *International Conference on Medical Imaging with Deep Learning*, pp. 285–296.
- Krähenbühl, P., Koltun, V., 2011. Efficient inference in fully connected crfs

- with gaussian edge potentials, in: *Advances in neural information processing systems*, pp. 109–117.
- Kuo, W., Häne, C., Yuh, E., Mukherjee, P., Malik, J., 2018. Cost-sensitive active learning for intracranial hemorrhage detection, in: *International Conference on Medical Image Computing and Computer-Assisted Intervention*, Springer. pp. 715–723.
- Larrazabal, A.J., Martinez, C., Ferrante, E., 2019. Anatomical priors for image segmentation via post-processing with denoising autoencoders, in: Shen, D., Liu, T., Peters, T.M., Staib, L.H., Essert, C., Zhou, S., Yap, P.T., Khan, A. (Eds.), *Medical Image Computing and Computer Assisted Intervention – MICCAI 2019*, Springer International Publishing. pp. 585–593.
- Li, M., Zhang, W., Yang, G., Wang, C., Zhang, H., Liu, H., Zheng, W., Li, S., 2019a. Recurrent Aggregation Learning for Multi-View Echocardiographic Sequences Segmentation. arXiv:1907.11292 [cs, eess] URL: <http://arxiv.org/abs/1907.11292>. arXiv: 1907.11292.
- Li, X., Chen, H., Qi, X., Dou, Q., Fu, C.W., Heng, P.A., 2018. H-denseunet: hybrid densely connected unet for liver and tumor segmentation from ct volumes. *IEEE transactions on medical imaging* 37, 2663–2674.
- Li, X., Yu, L., Chen, H., Fu, C.W., Heng, P.A., 2019b. Transformation consistent self-ensembling model for semi-supervised medical image segmentation. arXiv preprint arXiv:1903.00348 .
- Li, Z., Kamnitsas, K., Glocker, B., 2019c. Overfitting of neural nets under class imbalance: Analysis and improvements for segmentation, in: *International Conference on Medical Image Computing and Computer-Assisted Intervention*, Springer. pp. 402–410.
- Liskowski, P., Krawiec, K., 2016. Segmenting retinal blood vessels with deep neural networks. *IEEE transactions on medical imaging* 35, 2369–2380.
- Litjens, G., Kooi, T., Bejnordi, B.E., Setio, A.A.A., Ciompi, F., Ghafoorian, M., Van Der Laak, J.A., Van Ginneken, B., Sánchez, C.I., 2017. A survey on deep learning in medical image analysis. *Medical image analysis* 42, 60–88.
- Liu, S., Xu, D., Zhou, S.K., Pauly, O., Grbic, S., Mertelmeier, T., Wicklein, J., Jerebko, A., Cai, W., Comaniciu, D., 2018. 3d anisotropic hybrid network: Transferring convolutional features from 2d images to 3d anisotropic volumes, in: *International Conference on Medical Image Computing and Computer-Assisted Intervention*, Springer. pp. 851–858.
- Ma, C., Ji, Z., Gao, M., 2019. Neural style transfer improves 3d cardiovascular mr image segmentation on inconsistent data, in: *International Conference on Medical Image Computing and Computer-Assisted Intervention*, Springer. pp. 128–136.
- Mahapatra, D., Bozorgtabar, B., Thiran, J.P., Reyes, M., 2018. Efficient active learning for image classification and segmentation using a sample selection and conditional generative adversarial network, in: *International Conference on Medical Image Computing and Computer-Assisted Intervention*, Springer. pp. 580–588.
- Matuszewski, D.J., Sintorn, I.M., 2018. Minimal annotation training for segmentation of microscopy images, in: *2018 IEEE 15th International Symposium on Biomedical Imaging (ISBI 2018)*, IEEE. pp. 387–390.
- Mehta, S., Mercan, E., Bartlett, J., Weave, D., Elmore, J.G., Shapiro, L., 2018. Y-Net: Joint Segmentation and Classification for Diagnosis of Breast Biopsy Images. arXiv:1806.01313 [cs] URL: <http://arxiv.org/abs/1806.01313>. arXiv: 1806.01313.
- Menze, B.H., Jakab, A., Bauer, S., Kalpathy-Cramer, J., Farahani, K., Kirby, J., Burren, Y., Porz, N., Slotboom, J., Wiest, R., et al., 2014. The multimodal brain tumor image segmentation benchmark (brats). *IEEE transactions on medical imaging* 34, 1993–2024.
- Milletari, F., Navab, N., Ahmadi, S.A., 2016. V-net: Fully convolutional neural networks for volumetric medical image segmentation, in: *2016 Fourth International Conference on 3D Vision (3DV)*, IEEE. pp. 565–571.
- Min, S., Chen, X., Zha, Z.J., Wu, F., Zhang, Y., 2018. A two-stream mutual attention network for semi-supervised biomedical segmentation with noisy labels. arXiv preprint arXiv:1807.11719 .
- Mirikharaji, Z., Hamarneh, G., 2018. Star shape prior in fully convolutional networks for skin lesion segmentation, in: *International Conference on Medical Image Computing and Computer-Assisted Intervention*, Springer. pp. 737–745.
- Mirikharaji, Z., Yan, Y., Hamarneh, G., 2019. Learning to segment skin lesions from noisy annotations. arXiv preprint arXiv:1906.03815 .
- Mondal, A.K., Dolz, J., Desrosiers, C., 2018. Few-shot 3d multi-modal medical image segmentation using generative adversarial learning. arXiv preprint arXiv:1810.12241 .
- Monteiro, M., Figueiredo, M.A., Oliveira, A.L., 2018. Conditional random fields as recurrent neural networks for 3d medical imaging segmentation. arXiv preprint arXiv:1807.07464 .
- Myronenko, A., 2018. 3d MRI brain tumor segmentation using autoencoder regularization. arXiv:1810.11654 [cs, q-bio] URL: <http://arxiv.org/abs/1810.11654>. arXiv: 1810.11654.
- Nie, D., Gao, Y., Wang, L., Shen, D., 2018. Asdnet: Attention based semi-supervised deep networks for medical image segmentation, in: Frangi, A.F., Schnabel, J.A., Davatzikos, C., Alberola-López, C., Fichtinger, G. (Eds.), *Medical Image Computing and Computer Assisted Intervention – MICCAI 2018*, Springer International Publishing, Cham. pp. 370–378.
- Oktay, O., Ferrante, E., Kamnitsas, K., Heinrich, M., Bai, W., Caballero, J., Cook, S.A., De Marvao, A., Dawes, T., O’Regan, D.P., et al., 2017. Anatomically constrained neural networks (acnns): application to cardiac image enhancement and segmentation. *IEEE transactions on medical imaging* 37, 384–395.
- Oktay, O., Schlemper, J., Folgoc, L.L., Lee, M., Heinrich, M., Misawa, K., Mori, K., McDonagh, S., Hammerla, N.Y., Kainz, B., Glocker, B., Rueckert, D., 2018. Attention U-Net: Learning Where to Look for the Pancreas. arXiv:1804.03999 [cs] URL: <http://arxiv.org/abs/1804.03999>. arXiv: 1804.03999.
- Ozdemir, F., Peng, Z., Tanner, C., Fuernstahl, P., Goksel, O., 2018. Active learning for segmentation by optimizing content information for maximal entropy, in: *Deep Learning in Medical Image Analysis and Multimodal Learning for Clinical Decision Support*. Springer, pp. 183–191.
- Panfilov, E., Tiulpin, A., Klein, S., Nieminen, M.T., Saarakkala, S., 2019. Improving robustness of deep learning based knee mri segmentation: Mixup and adversarial domain adaptation, in: *Proceedings of the IEEE International Conference on Computer Vision Workshops*, pp. 0–0.
- Qin, X., 2019. Transfer learning with edge attention for prostate mri segmentation. arXiv preprint arXiv:1912.09847 .
- Radosavovic, I., Dollár, P., Girshick, R., Gkioxari, G., He, K., 2018. Data distillation: Towards omni-supervised learning, in: *Proceedings of the IEEE Conference on Computer Vision and Pattern Recognition*, pp. 4119–4128.
- Ravishanker, H., Venkataramani, R., Thiruvengadam, S., Sudhakar, P., Vaidya, V., 2017. Learning and incorporating shape models for semantic segmentation, in: *International Conference on Medical Image Computing and Computer-Assisted Intervention*, Springer. pp. 203–211.
- Ronneberger, O., Fischer, P., Brox, T., 2015. U-Net: Convolutional Networks for Biomedical Image Segmentation. arXiv:1505.04597 [cs] URL: <http://arxiv.org/abs/1505.04597>. arXiv: 1505.04597.
- Ross, T., Zimmerer, D., Vemuri, A., Isensee, F., Wiesenfarth, M., Bodenstedt, S., Both, F., Kessler, P., Wagner, M., Müller, B., et al., 2018. Exploiting the potential of unlabeled endoscopic video data with self-supervised learning. *International journal of computer assisted radiology and surgery* , 1–9.
- Roth, H.R., Lu, L., Farag, A., Shin, H.C., Liu, J., Turkbey, E.B., Summers, R.M., 2015. Deeporgan: Multi-level deep convolutional networks for automated pancreas segmentation, in: *International conference on medical image computing and computer-assisted intervention*, Springer. pp. 556–564.
- Roy, A.G., Navab, N., Wachinger, C., 2018. Concurrent spatial and channel squeeze & excitation in fully convolutional networks, in: *International Conference on Medical Image Computing and Computer-Assisted Intervention*, Springer. pp. 421–429.
- Sakinis, T., Milletari, F., Roth, H., Korfiatis, P., Kostandy, P., Philbrick, K., Akkus, Z., Xu, Z., Xu, D., Erickson, B.J., 2019. Interactive segmentation of medical images through fully convolutional neural networks. arXiv preprint arXiv:1903.08205 .
- Schwing, A.G., Urtasun, R., 2015. Fully connected deep structured networks. arXiv preprint arXiv:1503.02351 .
- Sedai, S., Mahapatra, D., Hewavitharanage, S., Maetschke, S., Garnavi, R., 2017. Semi-supervised segmentation of optic cup in retinal fundus images using variational autoencoder, in: *International Conference on Medical Image Computing and Computer-Assisted Intervention*, Springer. pp. 75–82.
- Selvaraju, R.R., Cogswell, M., Das, A., Vedantam, R., Parikh, D., Batra, D., 2017. Grad-cam: Visual explanations from deep networks via gradient-based localization, in: *Proceedings of the IEEE International Conference on Computer Vision*, pp. 618–626.
- Shin, H.C., Roth, H.R., Gao, M., Lu, L., Xu, Z., Nogues, I., Yao, J., Mollura, D., Summers, R.M., 2016. Deep convolutional neural networks for computer-aided detection: Cnn architectures, dataset characteristics and transfer learning. *IEEE transactions on medical imaging* 35, 1285–1298.

- Shin, H.C., Tenenholtz, N.A., Rogers, J.K., Schwarz, C.G., Senjem, M.L., Gunter, J.L., Andriole, K.P., Michalski, M., 2018. Medical image synthesis for data augmentation and anonymization using generative adversarial networks, in: International Workshop on Simulation and Synthesis in Medical Imaging, Springer. pp. 1–11.
- Shorten, C., Khoshgoftaar, T.M., 2019. A survey on image data augmentation for deep learning. *Journal of Big Data* 6, 60.
- Silvestri, G., Antiga, L., 2018. Stereology as weak supervision for medical image segmentation.
- Sirinukunwattana, K., Pluim, J.P., Chen, H., Qi, X., Heng, P.A., Guo, Y.B., Wang, L.Y., Matuszewski, B.J., Bruni, E., Sanchez, U., et al., 2017. Gland segmentation in colon histology images: The glas challenge contest. *Medical image analysis* 35, 489–502.
- Sourati, J., Gholipour, A., Dy, J.G., Kurugol, S., Warfield, S.K., 2018. Active deep learning with fisher information for patch-wise semantic segmentation, in: *Deep Learning in Medical Image Analysis and Multimodal Learning for Clinical Decision Support*. Springer, pp. 83–91.
- Sourati, J., Gholipour, A., Dy, J.G., Tomas-Fernandez, X., Kurugol, S., Warfield, S.K., 2019. Intelligent labeling based on fisher information for medical image segmentation using deep learning. *IEEE transactions on medical imaging*.
- Spitzer, H., Kiwitz, K., Amunts, K., Harmeling, S., Dickscheid, T., 2018. Improving cytoarchitectonic segmentation of human brain areas with self-supervised siamese networks, in: *International Conference on Medical Image Computing and Computer-Assisted Intervention*, Springer. pp. 663–671.
- Sun, J., Shi, Y., Gao, Y., Wang, L., Zhou, L., Yang, W., Shen, D., 2018a. Interactive medical image segmentation via point-based interaction and sequential patch learning. *arXiv preprint arXiv:1804.10481*.
- Sun, L., Fan, Z., Huang, Y., Ding, X., Paisley, J., 2018b. Joint CS-MRI Reconstruction and Segmentation with a Unified Deep Network. *arXiv:1805.02165 [cs]* URL: <http://arxiv.org/abs/1805.02165>. *arXiv:1805.02165*.
- Taghanaki, S.A., Abhishek, K., Cohen, J.P., Cohen-Adad, J., Hamarneh, G., 2019. Deep semantic segmentation of natural and medical images: A review. *arXiv preprint arXiv:1910.07655*.
- Tajbakhsh, N., Hu, Y., Cao, J., Yan, X., Xiao, Y., Lu, Y., Liang, J., Terzopoulos, D., Ding, X., 2019a. Surrogate supervision for medical image analysis: Effective deep learning from limited quantities of labeled data. *arXiv preprint arXiv:1901.08707*.
- Tajbakhsh, N., Lai, B., Ananth, S., Ding, X., 2019b. Erronet: Learning error representations from limited data to improve vascular segmentation. *arXiv preprint arXiv:1910.04814*.
- Tajbakhsh, N., Shin, J.Y., Gurudu, S.R., Hurst, R.T., Kendall, C.B., Gotway, M.B., Liang, J., 2016. Convolutional neural networks for medical image analysis: Full training or fine tuning? *IEEE transactions on medical imaging* 35, 1299–1312.
- Tang, Y., Cai, J., Lu, L., Harrison, A.P., Yan, K., Xiao, J., Yang, L., Summers, R.M., 2018. Ct image enhancement using stacked generative adversarial networks and transfer learning for lesion segmentation improvement, in: *International Workshop on Machine Learning in Medical Imaging*, Springer. pp. 46–54.
- Tang, Y., Tang, Y., Xiao, J., Summers, R.M., 2019a. Xlsor: A robust and accurate lung segmentor on chest x-rays using criss-cross attention and customized radiorealistic abnormalities generation. *arXiv preprint arXiv:1904.09229*.
- Tang, Y.B., Oh, S., Tang, Y.X., Xiao, J., Summers, R.M., 2019b. Ct-realistic data augmentation using generative adversarial network for robust lymph node segmentation, in: *Medical Imaging 2019: Computer-Aided Diagnosis*, International Society for Optics and Photonics. p. 109503V.
- Valindria, V.V., Pawlowski, N., Rajchl, M., Lavdas, I., Aboagye, E.O., Rockall, A.G., Rueckert, D., Glocker, B., 2018. Multi-modal learning from unpaired images: Application to multi-organ segmentation in CT and MRI. *Proceedings - 2018 IEEE Winter Conference on Applications of Computer Vision, WACV 2018 2018-Janua*, 547–556. doi:10.1109/WACV.2018.00066.
- Veeling, B.S., Linmans, J., Winkens, J., Cohen, T., Welling, M., 2018. Rotation equivariant cnns for digital pathology, in: *International Conference on Medical image computing and computer-assisted intervention*, Springer. pp. 210–218.
- Verma, V., Lamb, A., Beckham, C., Najafi, A., Mitliagkas, I., Lopez-Paz, D., Bengio, Y., 2019. Manifold mixup: Better representations by interpolating hidden states, in: *International Conference on Machine Learning*, pp. 6438–6447.
- Wachinger, C., Reuter, M., Klein, T., 2018. Deepnat: Deep convolutional neural network for segmenting neuroanatomy. *NeuroImage* 170, 434–445.
- Wang, G., Li, W., Zuluaga, M.A., Pratt, R., Patel, P.A., Aertsen, M., Doel, T., David, A.L., Deprest, J., Ourselin, S., et al., 2018a. Interactive medical image segmentation using deep learning with image-specific fine tuning. *IEEE transactions on medical imaging* 37, 1562–1573.
- Wang, G., Zuluaga, M.A., Li, W., Pratt, R., Patel, P.A., Aertsen, M., Doel, T., David, A.L., Deprest, J., Ourselin, S., et al., 2018b. Deepigeos: a deep interactive geodesic framework for medical image segmentation. *IEEE transactions on pattern analysis and machine intelligence*.
- Wang, S., Zhou, M., Gevaert, O., Tang, Z., Dong, D., Liu, Z., Tian, J., 2017. A multi-view deep convolutional neural networks for lung nodule segmentation, in: *2017 39th Annual International Conference of the IEEE Engineering in Medicine and Biology Society (EMBC)*, IEEE. pp. 1752–1755.
- Xia, Y., Liu, F., Yang, D., Cai, J., Yu, L., Zhu, Z., Xu, D., Yuille, A., Roth, H., 2020. 3d semi-supervised learning with uncertainty-aware multi-view co-training.
- Xia, Y., Xie, L., Liu, F., Zhu, Z., Fishman, E.K., Yuille, A.L., 2018. Bridging the gap between 2d and 3d organ segmentation with volumetric fusion net, in: *International Conference on Medical Image Computing and Computer-Assisted Intervention*, Springer. pp. 445–453.
- Xu, Z., Niethammer, M., 2019. Deepatlas: Joint semi-supervised learning of image registration and segmentation, in: *Medical Image Computing and Computer Assisted Intervention (MICCAI)*, Springer. pp. 420–429.
- Yan, K., Wang, X., Lu, L., Summers, R.M., 2018. Deeplesion: automated mining of large-scale lesion annotations and universal lesion detection with deep learning. *Journal of medical imaging* 5, 036501.
- Yang, L., Zhang, Y., Chen, J., Zhang, S., Chen, D.Z., 2017. Suggestive annotation: A deep active learning framework for biomedical image segmentation, in: *International conference on medical image computing and computer-assisted intervention*, Springer. pp. 399–407.
- Yi, X., Walia, E., Babyn, P., 2018. Generative adversarial network in medical imaging: A review. *arXiv preprint arXiv:1809.07294*.
- Yu, L., Wang, S., Li, X., Fu, C.W., Heng, P.A., 2019. Uncertainty-aware self-ensembling model for semi-supervised 3d left atrium segmentation, in: *International Conference on Medical Image Computing and Computer-Assisted Intervention*, Springer. pp. 605–613.
- Yu, Q., Xie, L., Wang, Y., Zhou, Y., Fishman, E.K., Yuille, A.L., 2018. Recurrent saliency transformation network: Incorporating multi-stage visual cues for small organ segmentation, in: *Proceedings of the IEEE Conference on Computer Vision and Pattern Recognition*, pp. 8280–8289.
- Zhang, C., Bengio, S., Hardt, M., Recht, B., Vinyals, O., 2016. Understanding deep learning requires rethinking generalization. *arXiv preprint arXiv:1611.03530*.
- Zhang, H., Cisse, M., Dauphin, Y.N., Lopez-Paz, D., 2018a. mixup: Beyond empirical risk minimization. *International Conference on Learning Representations* URL: <https://openreview.net/forum?id=r1Ddp1-Rb>.
- Zhang, L., Gopalakrishnan, V., Lu, L., Summers, R.M., Moss, J., Yao, J., 2018b. Self-learning to detect and segment cysts in lung ct images without manual annotation, in: *2018 IEEE 15th International Symposium on Biomedical Imaging (ISBI 2018)*, IEEE. pp. 1100–1103.
- Zhang, L., Wang, X., Yang, D., Sanford, T., Harmon, S., Turkbey, B., Roth, H., Myronenko, A., Xu, D., Xu, Z., 2019a. When unseen domain generalization is unnecessary? rethinking data augmentation. *arXiv preprint arXiv:1906.03347*.
- Zhang, P., Wang, F., Zheng, Y., 2017a. Self supervised deep representation learning for fine-grained body part recognition, in: *2017 IEEE 14th International Symposium on Biomedical Imaging (ISBI 2017)*, IEEE. pp. 578–582.
- Zhang, P., Zhong, Y., Deng, Y., Tang, X., Li, X., 2019b. A survey on deep learning of small sample in biomedical image analysis. *arXiv preprint arXiv:1908.00473*.
- Zhang, Y., Miao, S., Mansi, T., Liao, R., 2018c. Task driven generative modeling for unsupervised domain adaptation: Application to x-ray image segmentation, in: *International Conference on Medical Image Computing and Computer-Assisted Intervention*, Springer. pp. 599–607.
- Zhang, Y., Yang, L., Chen, J., Fredericksen, M., Hughes, D.P., Chen, D.Z., 2017b. Deep adversarial networks for biomedical image segmentation utilizing unannotated images, in: *Descoteaux, M., Maier-Hein, L., Franz, A., Jannin, P., Collins, D.L., Duchesne, S. (Eds.), Medical Image Computing*

- and Computer Assisted Intervention – MICCAI 2017, Springer International Publishing, Cham. pp. 408–416.
- Zhang, Y., Yang, Q., 2017. A Survey on Multi-Task Learning. arXiv:1707.08114 [cs] URL: <http://arxiv.org/abs/1707.08114>. arXiv: 1707.08114.
- Zhang, Z., Li, J., Zhong, Z., Jiao, Z., Gao, X., 2019c. A sparse annotation strategy based on attention-guided active learning for 3d medical image segmentation. arXiv preprint arXiv:1906.07367 .
- Zhang, Z., Yang, L., Zheng, Y., 2018d. Translating and segmenting multimodal medical volumes with cycle-and shape-consistency generative adversarial network, in: Proceedings of the IEEE Conference on Computer Vision and Pattern Recognition, pp. 9242–9251.
- Zhao, A., Balakrishnan, G., Durand, F., Guttag, J.V., Dalca, A.V., 2019a. Data augmentation using learned transforms for one-shot medical image segmentation. arXiv preprint arXiv:1902.09383 .
- Zhao, Y.X., Zhang, Y.M., Song, M., Liu, C.L., 2019b. Multi-view semi-supervised 3d whole brain segmentation with a self-ensemble network, in: International Conference on Medical Image Computing and Computer-Assisted Intervention, Springer. pp. 256–265.
- Zheng, H., Yang, L., Chen, J., Han, J., Zhang, Y., Liang, P., Zhao, Z., Wang, C., Chen, D.Z., 2019. Biomedical image segmentation via representative annotation .
- Zheng, S., Jayasumana, S., Romera-Paredes, B., Vineet, V., Su, Z., Du, D., Huang, C., Torr, P.H., 2015. Conditional random fields as recurrent neural networks, in: Proceedings of the IEEE international conference on computer vision, pp. 1529–1537.
- Zhou, B., Khosla, A., Lapedriza, A., Oliva, A., Torralba, A., 2016. Learning deep features for discriminative localization, in: Proceedings of the IEEE conference on computer vision and pattern recognition, pp. 2921–2929.
- Zhou, Y., Li, Z., Bai, S., Wang, C., Chen, X., Han, M., Fishman, E., Yuille, A., 2019a. Prior-aware neural network for partially-supervised multi-organ segmentation. arXiv preprint arXiv:1904.06346 .
- Zhou, Y., Wang, Y., Tang, P., Bai, S., Shen, W., Fishman, E.K., Yuille, A.L., 2018a. Semi-supervised multi-organ segmentation via deep multi-planar co-training. arXiv preprint arXiv:1804.02586 .
- Zhou, Z., Siddiquee, M.M.R., Tajbakhsh, N., Liang, J., 2018b. Unet++: A nested u-net architecture for medical image segmentation, in: Deep Learning in Medical Image Analysis and Multimodal Learning for Clinical Decision Support. Springer, pp. 3–11.
- Zhou, Z., Sodha, V., Rahman Siddiquee, M.M., Feng, R., Tajbakhsh, N., Gotway, M., Liang, J., 2019b. Models genesis: Generic autodidactic models for 3d medical image analysis, in: Medical Image Computing and Computer-Assisted Intervention (MICCAI). Springer International Publishing. URL: www.tinyurl.com/ModelsGenesisFullVersion.
- Zhu, H., Shi, J., Wu, J., 2019. Pick-and-learn: Automatic quality evaluation for noisy-labeled image segmentation, in: International Conference on Medical Image Computing and Computer-Assisted Intervention, Springer. pp. 576–584.
- Zhu, J.Y., Park, T., Isola, P., Efros, A.A., 2017. Unpaired image-to-image translation using cycle-consistent adversarial networks, in: Proceedings of the IEEE international conference on computer vision, pp. 2223–2232.
- Zhuang, X., Li, L., Payer, C., Štern, D., Urschler, M., Heinrich, M.P., Oster, J., Wang, C., Smedby, Ö., Bian, C., et al., 2019. Evaluation of algorithms for multi-modality whole heart segmentation: An open-access grand challenge. Medical image analysis 58, 101537.